Title

AAV-PHP.B Administration Results in a Differential Pattern of CNS Biodistribution in Non-human Primates Compared with Mice.

Journal

Molecular Therapy, 27(11)

Authors

Liguore, William

Domire, Jacqueline

Button, Dana

et al.

Publication Date

2019-11-06

DOI

10.1016/j.ymthe.2019.07.017

Peer reviewed

Molecular Therapy
Original Article

AAV-PHP.B Administration Results in a Differential Pattern of CNS Biodistribution in Non-human Primates Compared with Mice

William A. Liguore,[1] Jacqueline S. Domire,[1] Dana Button,[1] Yun Wang,[1] Brett D. Dufour,[1,2] Sathya Srinivasan,[1] and Jodi L. McBride[1,2]

[1]Division of Neuroscience, Oregon National Primate Research Center, Beaverton, OR, USA; [2]Department of Behavioral Neuroscience, Oregon Health and Science University, Portland, OR, USA

The ability of recombinant adeno-associated virus (AAV) to deliver transgenes to the CNS has allowed for several advancements in the field of gene therapy to treat brain disorders. Although most AAVs do not readily cross the blood-brain barrier and transduce the CNS following peripheral administration, AAV-PHP.B has recently been shown to transduce brains of mice with higher efficiency compared with its parent serotype, AAV9, following injection into the retro-orbital sinus. Here, we extended this foundational work by comparing AAV-PHP.B transduction efficiency in wild-type C57BL/6J mice using four clinically applicable delivery strategies including two intravascular (intra-jugular vein and intra-carotid artery) and two intra-cerebral spinal fluid (CSF) routes (intra-cisterna magna and intra-lateral ventricle). We scaled up these comparisons in a larger-animal model and evaluated transduction efficiency of AAV-PHP.B in the rhesus macaque. We found widespread and largely equal CNS transduction in mice following all four injection strategies, whereas we observed a differential pattern of transduction in macaques with broad cortical and spinal cord transduction seen after intrathecal administration and only very low transduction following intravascular administration. Taken together, these results suggest that AAV-PHP.B may be a useful gene therapy vector for neurological disorders, particularly those stemming from broad cortical or spinal cord neuropathology.

INTRODUCTION

The use of viral vectors to deliver genes to the brain and spinal cord has opened up great possibilities in the realm of both modeling and treating a variety of CNS disorders. Recombinant adeno-associated virus (rAAV) has emerged as a front-runner for both pre-clinical and clinical gene therapy studies because of its positive safety profile in both animal and human studies,[1] its ability to transduce several different cell types in the brain,[1–5] its maintenance of expression with low integration rates,[6–9] and its relative ease of production.[10–12] Historically, delivery of AAV to the brain has been achieved via stereotaxic, magnetic resonance imaging (MRI)-guided intraparenchymal injections into focal brain regions of interest, including several AAV-based therapeutic approaches that have made their way into clinical trials for neurological disorders including Canavan's,[13] Parkinson's,[14–17] and Alzheimer's[18] diseases (ADs), as well as lysosomal storage disorders (LSDs), including late infantile neuronal ceroid lipofuscinoses (CLN2 variant)[19] and mucopolysaccharidosis III.[20] Similarly, AAV-based gene therapies to treat eye disorders have seen incredible advancements over the past several years, with ongoing clinical trials for Leber congenital amaurosis, age-related macular degeneration, achromatopsia, and choroideremia, as well as the landmark US Food and Drug Administration approval of voretigene neparvovec-rzyl (tradename: Luxturna) in late 2017, an AAV-based therapy for patients suffering from RPE65 mutation-associated retinal dystrophy.[21]

Despite these advances, delivering genetic material efficiently to the CNS still remains a hurdle in developing efficacious gene therapy strategies for CNS disorders characterized by widespread neuropathology throughout several brain regions where a focal, targeted gene delivery is far less likely to be efficacious. Although the majority of the AAV serotypes identified to date show poor efficiency in crossing the blood-brain barrier (BBB) when administered peripherally, a pivotal study in 2009 by Foust et al.[22] found that rAAV serotype 9 (AAV9) crosses the BBB from an intravenous (i.v.) injection and transduces neurons and glia throughout the brain, spinal cord, and in multiple peripheral tissues. Since that discovery, numerous laboratories have demonstrated that AAV9 can deliver therapeutic cargo across the BBB from an i.v. injection or throughout the CNS from an intra-cerebral spinal fluid (CSF) infusion, partially correcting phenotypes in some CNS disease models including LSDs,[23–29] Rett syndrome (RS),[30,31] spinal muscular atrophy (SMA),[32–35] amyotrophic lateral sclerosis (ALS),[36–38] and AD.[39] Encouragingly, a few of these AAV9-based gene therapy programs have recently progressed to clinical trials for neurological disorders, including those for SMA types 1

Received 4 January 2019; accepted 26 July 2019;
https://doi.org/10.1016/j.ymthe.2019.07.017.

Correspondence: Jodi L. McBride, PhD, Division of Neuroscience, Oregon National Primate Research Center, 505 NW 185th Avenue, Beaverton, OR 97006, USA.
E-mail: mcbridej@ohsu.edu

Table 1. Study Participants

Species	Age at Administration	Dose (Total VGs)	VG/kg Body Weight	Volume of Infusion	Route of Administration	No. of Animals Per Group
Mouse	12–16 weeks	3e10	1.5e12	60 μL	jugular vein	8
Mouse	12–16 weeks	3e10	1.5e12	60 μL	internal carotid artery	8
Mouse	12–16 weeks	3e10	1.5e12	15 μL	lateral ventricle	8
Mouse	12–16 weeks	3e10	1.5e12	15 μL	cisterna magna	8
Mouse	12–16 weeks	1e11	5e12	60 μL	jugular vein	8
Mouse	12–16 weeks	1e11	5e12	60 μL	internal carotid artery	8
Rhesus macaque	1–2 years	2e12	1e12	2 mL	internal carotid artery	2
Rhesus macaque	1–2 years	2e12	1e12	2 mL	cisterna magna	2

The study participants for both the mouse and NHP studies are detailed. For mouse studies, n = 3 animals per group were used for vector genome copy studies and n = 5 animals per group were used for immunofluorescent studies (n = 8 total per group). Dose per kilogram listed for the mouse studies (for comparison with published data) is estimated based on an average weight of 20 g per mouse; however, mice were all dosed with the same total viral genome number. All mice used in this study were C57BL/6J. For NHP studies, n = 2 juvenile rhesus macaques per group were used for both vector genome copy analysis and immunofluorescent studies. Dose per kilogram listed for the NHP studies (for comparison with published data) is estimated based on an average weight of 2 kg per NHP; however, NHPs were all dosed with the same total viral genome number. All NHPs used in this study were rhesus macaques of Indian origin. VG, vector genome.

and 2 (ClinicalTrials.gov: NCT02122952 and NCT03381729) and CLN6 Batten disease (ClinicalTrials.gov: NCT02725580).

Although global CNS gene delivery has made significant progress in the last decade, the transduction efficiency of AAVs that cross the BBB and target widespread regions of the brain still remains quite low in comparison with transduction efficiencies achieved from direct brain injections.[22,40] New AAV capsid mutants have been engineered by several groups by utilizing rational design or via molecular evolution technology in an attempt to enhance transduction efficiency in brain tissue, including work by Deverman et al.,[41] who used a Cre-dependent evolution approach to generate an AAV9 capsid mutant named AAV-PHP.B. This novel AAV capsid contains a 7-amino acid (aa) insertion in the VP1 capsid protein between aa 588 and 589, and is distinguished from its template serotype by its propensity to cross the BBB and transduce CNS cells with a 40-fold greater efficiency than AAV9 without significant increases in peripheral organ transduction. To characterize the transduction profile of this novel serotype, Deverman et al.[41] administered AAV-PHP.B into the retro-orbital sinus, a venous reservoir located behind the rodent eye, and assessed EGFP expression and vector genome (VG) copy number throughout the brain and periphery of C57BL/6J wild-type mice.

Although the retro-orbital sinus, facial vein, and tail vein are commonly used sites of intravascular injection in rodent gene therapy studies, particularly for their ease of access, these delivery approaches are undoubtedly less translatable compared with approaches that will be scaled up in large-animal model studies and ultimately evaluated in human patient populations. Therefore, in the current study, we extended the foundational work by Deverman et al.[41] by investigating the transduction efficiency of AAV-PHP.B in mice using two clinically applicable intravascular surgical approaches: intra-jugular vein and intra-internal carotid artery administration. In human patient populations, these intravascular approaches are typically achieved via the placement of central lines or remote catheterization under image guidance and have been used successfully to deliver drugs to the CNS, including chemotherapy agents.[42–44] These vascular delivery modalities, particularly the internal carotid artery infusions, were chosen to maximize first-pass delivery of AAV-PHP.B to the brain. Moreover, we directly compared these two vascular delivery approaches with two clinically feasible intra-CSF approaches in mice by injecting AAV-PHP.B into either the intracerebroventricular (i.c.v.) space of the lateral ventricle or into the intrathecal (i.t.) space of the cisterna magna via a suboccipital puncture. The rationale for directly comparing i.v. approaches with intra-CSF approaches using AAV-PHP.B was based on the recent success of i.t. administration of AAV9 in delivering therapeutic genes throughout the brain and spinal cord in pre-clinical studies for a variety of neurological disorders.[45–52] In addition to studies in mice, we scaled up our investigation in a large-animal model by characterizing the biodistribution of AAV-PHP.B in the rhesus macaque and directly compared transduction efficiency throughout the brain, spinal cord, and in peripheral tissues following intra-arterial (internal carotid artery) or intrathecal (cisterna magna) administration. Together, this work investigates the safety and utility of using AAV-PHP.B to deliver genes throughout the mouse and primate CNS for a variety of neurological disorders that would benefit from a widespread gene therapy approach.

RESULTS

Direct Comparison of Four Clinically Relevant Administration Routes of AAV-PHP.B in C57BL/6J Mice

We first investigated the transduction efficiency in the brain of AAV-PHP.B-expressing EGFP (AAV-PHP.B-EGFP) in wild-type adult C57BL/6J mice at a dose of 3E10 VGs or 1.5E12 VGs/kilogram body weight (VG/kg). See Table 1 for a list of study participant information including ages, groups, doses, and volumes of infusion. We compared transduction efficiencies between the four administration routes by using immunofluorescent (IF) staining for EGFP to characterize biodistribution of AAV.PHP.B throughout the brain.

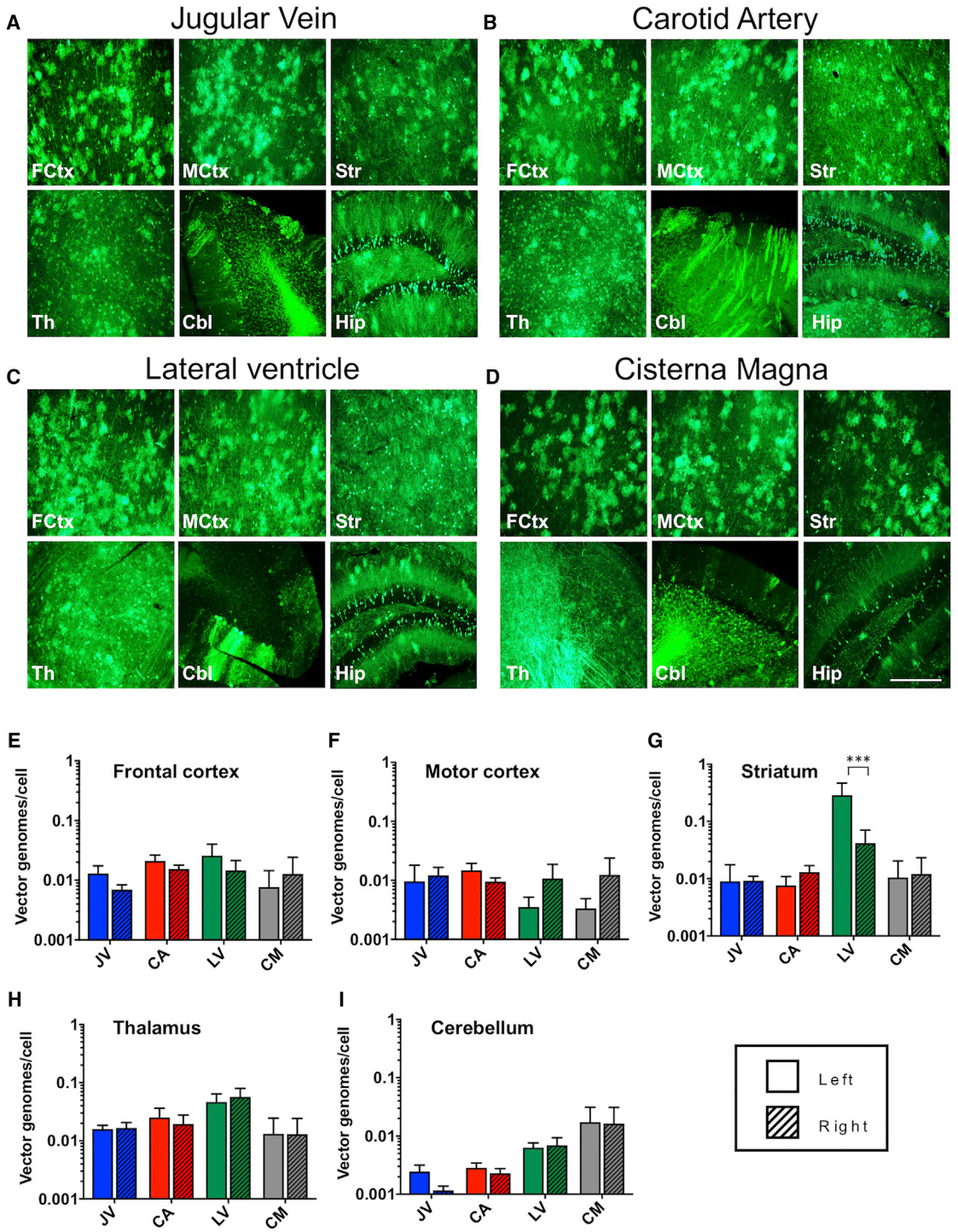

Figure 1. Comparison of Four Injection Routes of AAV-PHP.B in Mice at a Dose of 3E10 VGs

(A–D) High-power photomicrographs imaged with a ×20 objective and extended field image function show AAV-PHP.B transduction of six regions throughout the mouse brain (n = 5 mice imaged per injection group). Mouse brain transduction in four administration routes are shown: jugular vein (A), carotid artery (B), lateral ventricle (C), and cisterna magna (D). Brain regions are (clockwise from upper left) frontal cortex (FCtx), motor cortex (MCtx), striatum (Str), hippocampus (Hip), cerebellum (Cbl), and thalamus (Th). Scale bar in (D) represents 500 μm and applies to all photomicrographs. (E–I) AAV-PHP.B vector genome copy data of left and right hemispheres for the 3E10 VG dose

(legend continued on next page)

Additionally, in a second cohort of injected animals, we dissected five brain regions from both hemispheres including the frontal and motor cortices, striatum, thalamus, and cerebellum, and quantitated the number of AAV-PHP.B VG copies (VGCs) per cell in each region using qPCR. As part of this analysis, we were also interested in investigating potential differences in transduction between hemispheres, given that three out of four of our injection paradigms were administered unilaterally, including the jugular vein, carotid artery, and lateral ventricle. The cisterna magna infusion was positioned centrally in the cisternal space directly posterior to the cerebellum.

We detected widespread EGFP expression throughout the brain in mice from each of the four injection groups. $EGFP^+$ cells were observed throughout many regions of the cerebral cortex (Figures 1A–1D, top, left, and center panels, examples from the frontal and motor cortices). $EGFP^+$ neurons and glia were found throughout all cortical layers, with no discernable differences between injection routes or between hemispheres. $EGFP^+$ neurons and glia were also observed throughout the rostral-to-caudal extent of the striatum in each injection group (Figures 1A–1D, top right panels). $EGFP^+$ fibers were also abundant in the striatum, potentially reflecting fibers from transduced cells in afferent brain regions including the cortex and thalamus. We detected a notable difference in hemispheric EGFP expression in the striatum, with the left hemisphere showing higher expression compared with the right hemisphere, in mice infused into the left lateral ventricle. However, none of the other injection routes led to a difference in laterality in the striatum or any other brain region. The thalamus contained abundant $EGFP^+$ neurons and glia in all injection routes, and we observed a particularly high number of EGFP fibers in this region following injection into the cisterna magna (Figure 1D, bottom left panel). Transduction in the cerebellum was characterized by $EGFP^+$ neurons and glia in both cerebellar cortex and deep cerebellar nuclei following all injection routes (Figures 1A–1D, bottom center panels), with the highest expression resulting from injection into the cisterna magna. We also noted very robust expression of EGFP throughout the hippocampus, particularly in the dentate gyrus, following each administration route (Figures 1A–1D, bottom right panel).

To quantify and compare the efficiency of gene transfer between administration routes, we assessed vector genome copy (VGC) numbers per cell in several brain regions via qPCR. The range of VGCs that we detected, including all injection routes, was 0.008–0.026 VGC/cell for the left hemisphere and 0.007–0.015 VGC/cell for the right hemisphere of the frontal cortex (Figure 1E), 0.003–0.015 VGC/cell for the left hemisphere and 0.01–0.013 VGC/cell for the right hemisphere of the motor cortex (Figure 1F), 0.008–0.289 VGC/cell for the left hemisphere and 0.009–0.042 VGC/cell for the right hemisphere of the striatum (Figure 1G), 0.013–0.047 VGC/cell for the left hemisphere and 0.013–0.057 VGC/cell for the right hemisphere of the thalamus (Figure 1H), and 0.003–0.017 VGC/cell for the left hemisphere and 0.001–0.016 VGC/cell for the right hemisphere of the cerebellum (Figure 1I). A two-way ANOVA statistical analysis with brain region (left and right hemispheres) and injection route as the independent variables and VGC numbers as the dependent variable showed significant differences in the total number of VGCs per cell between injection routes [$F(3, 70) = 3.509$, $p = 0.0197$] without significant differences in VGCs per cell between brain regions [$F(9, 70) = 1.604$, $p = 0.1309$]. The interaction between route of injection and brain region was also significant [$F(27, 70) = 1.779$, $p = 0.0285$]. Significance based on injection route was largely driven by the increase in transduction in the left striatum following injection into the lateral ventricle in the ipsilateral hemisphere (Figure 1G). VGCs in the left striatum following a left ventricular injection were not only significantly higher compared with the right striatum, but also significantly different when compared with either hemisphere from all other brain regions from each injection route ($p < 0.001$ for all Tukey's post hoc comparisons). Interestingly, and contrary to our hypotheses, we detected no significant hemispheric differences in any brain region measured when comparing VGCs following injections into the jugular vein versus the internal carotid artery; VGC number was similar in left and right hemispheres in all regions measured ($p > 0.05$ for all comparisons; Figures 1E–1I).

AAV-PHP.B Cell Transduction Profile in Mouse Brain following Intravascular and Intra-CSF Delivery

We next used double-IF staining to identify the cellular transduction profiles in mice injected with AAV-PHP.B-EGFP at a dose of 3E10 VGs. We used an antibody directed against EGFP to detect all transduced cells and used antibodies against neuronal nuclear protein (NeuN) to detect neurons, glial fibrillary acidic protein (GFAP) to detect astrocytes, Olig2 for oligodendrocytes, CD31 for vascular endothelial cells, and Iba1 to label microglia. In mice from all four administration groups, AAV.PHP.B transduced neurons (Figures 2A–2F), astrocytes (Figures 2G–2L), oligodendrocytes (Figures 2M–2R), and vascular endothelial cells (Figures 2S–2X), but not microglia (data not shown), in widespread cortical and subcortical regions throughout the brain. Examples of double-labeled IF cells in Figure 2 are from the striatum (left panel) and motor cortex (right panel) of animals injected into the jugular vein. A qualitative analysis of transduction levels of each cell type in the striatum and motor cortex from mice in each injection group is in Table S1. In the striatum, the majority of $EGFP^+$/$NeuN^+$-labeled neurons had a characteristic shape of medium spiny neurons with extensive dendritic trees (Figures 2A–2C, white arrowheads), but we also detected sparse examples of larger, aspiny $EGFP^+$ striatal interneurons. $EGFP^+$/$NeuN^+$-labeled neurons in the motor cortex appeared to be primarily large multipolar pyramidal cells (Figures 2D–2F, white arrowheads). We detected considerably more

presented as mean ± SEM vector genomes per cell (n = 3 mice evaluated per group): frontal cortex (E), motor cortex (F), striatum (G), thalamus (H), and cerebellum (I). Statistical analysis revealed no differences in vector distribution between injection routes in most brain regions; however, significant laterality in the striatum was detected when delivering virus directly into the lateral ventricle of the same hemisphere ($p < 0.001$). CA, carotid artery; CM, cisterna magna; JV, jugular vein; LV, lateral ventricle. ***$p < 0.001$.

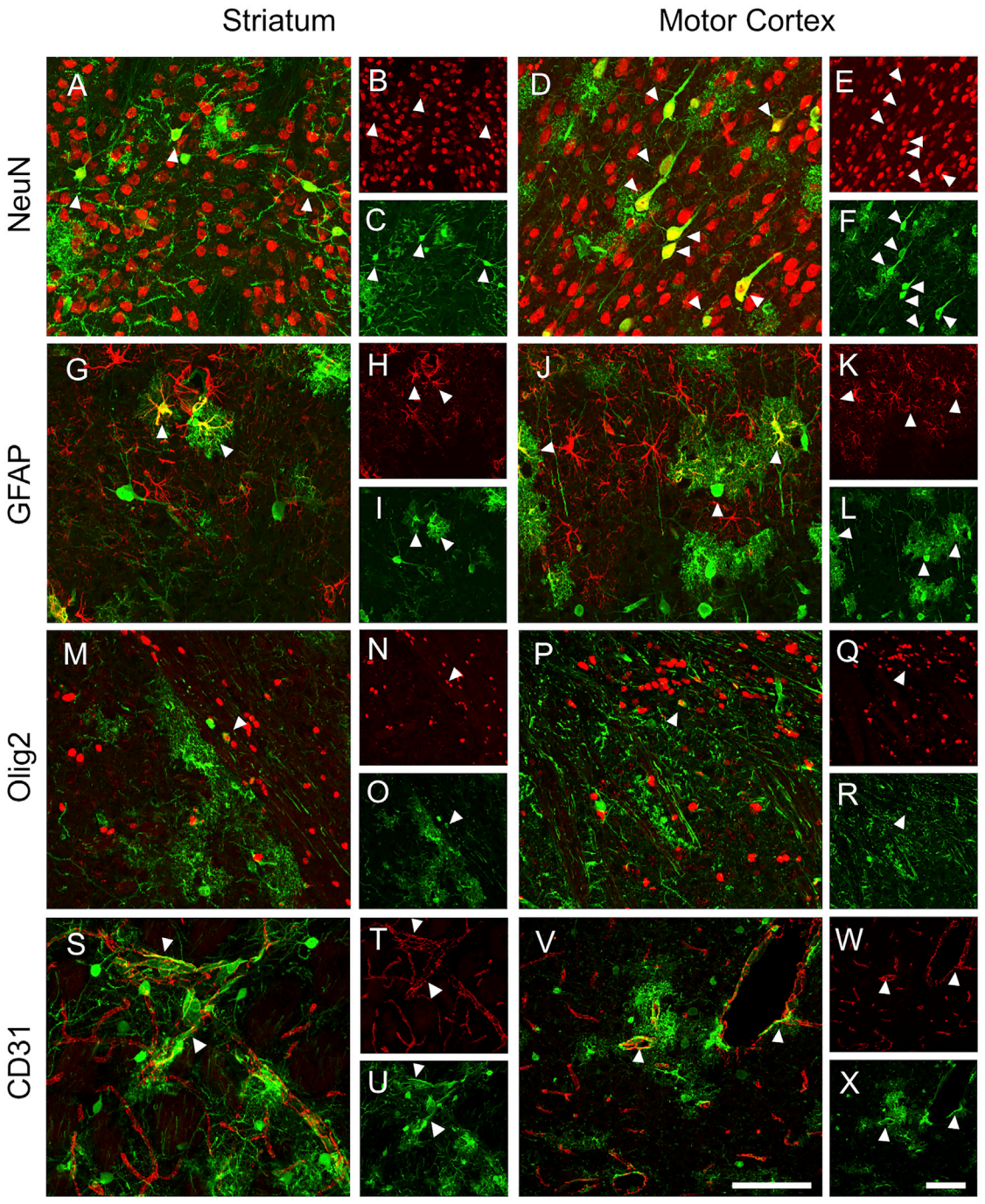

Figure 2. AAV-PHP.B Transduces Neurons, Astrocytes, Vascular Endothelial Cells, and Oligodendrocytes in the Mouse Brain

Double-labeled IF of AAV-PHP.B-transduced mouse neurons ($GFP^+/NeuN^+$, A–F), astrocytes ($GFP^+/GFAP^+$, G–L), oligodendrocytes ($GFP^+/Olig2^+$, M–R), and vascular endothelial cells ($GFP^+/CD31^+$, S–X). Examples were imaged from the mouse striatum (left panel) and motor cortex (right panel). In all cases, $EGFP^+$ cells are shown in green, the cell specific marker is shown in red, and the merged images are shown in the largest panel of the trio, with double-labeled cells in yellow. All cells were imaged using a confocal microscope at original magnification ×63 from mice injected into the jugular vein with 3E10 VGs of AAV-PHP.B (n = 5 mice imaged). AAV-PHP.B efficiently transduces neurons, astrocytes, oligodendrocytes, and vascular endothelial cells; however, examples of AAV-PHP.B-transduced $Iba1^+$ microglia were not detected (not shown). Scale bars represent 100 μm (V and X).

EGFP$^+$/GFAP$^+$-labeled astrocytes in the motor cortex compared with the striatum in each of the four administration groups (Figures 2G–2L; Table S1), a phenomenon that we have previously seen following injection of AAV9 into the jugular vein.[40] In both the striatum and motor cortex, we detected only a very low number of EGFP$^+$/Olig2$^+$ oligodendrocytes, with equal numbers detected regardless of the injection route (Figures 2M–2R; Table S1). Although we found transduced blood vessels in mice from all administration groups, we observed more EGFP$^+$/CD31$^+$-labeled vascular endothelial cells in mice injected into the jugular vein or internal carotid artery compared with mice injected via either of the intra-CSF routes, which was anticipated (Figures 2S–2X; Table S1). No EGFP$^+$/Iba1$^+$-labeled microglia were detected in any brain regions of any mice (data not shown).

Significant Dose-Dependent Increases following Both Venous and Arterial Delivery of AAV-PHP.B in Mice

To enhance transduction efficiency in the brain, we injected adult wild-type C57BL/6J mice with AAV-PHP.B at a dose 3.3× higher than in our first study cohort (1E11 VGs compared with 3E10 VGs). Mice were injected into either the jugular vein or the internal carotid artery; however, because of volume restrictions when administering into the CSF and the relatively low titer of our virus, we were unable to assess dose escalation via the two intra-CSF routes of administration. Mice injected with 1E11 VGs of AAV-PHP.B versus 3E10 VGs showed a distinct increase in EGFP IF throughout the entire rostral-to-caudal extent of the brain, with the same brain regions transduced in both comparison groups (Figure 3A). A more detailed, high-power panel of EGFP IF for individual brain regions injected at a dose of 1E11 VGs that corresponds to Figures 1A and 1B is shown in Figure S1.

Analysis of VGC number between hemispheres was non-significant, and therefore data from each hemisphere were averaged for further statistical analyses ($p > 0.05$ for each brain region and dose). A two-way ANOVA statistical analysis with brain region and injection route as the independent variables and VGC numbers as the dependent variable detected significant differences in the total number of VGCs between doses [$F(3,35) = 39.31$, $p < 0.0001$] and brain regions [$F(4,35) = 10.7$, $p < 0.0001$]. The interaction between dose and brain region was also significant [$F(12,35) = 2.248$, $p = 0.0310$]. We found a significant increase in the number of VGCs per cell in 1E11 VG-injected animals compared with 3E10 VG-injected animals in all brain regions analyzed except for the cerebellum, regardless of injection route (Tukey's post hoc comparisons, $p < 0.05$ in all cases; however, the graph in Figure 3B demonstrates statistical significance between high and low groups from the same injection route only). At the 1E11 dose, the range of VGCs per cell for each brain region was as follows: 0.071–0.104 VGCs/cell in the frontal cortex, 0.060–0.100 VGCs/cell in the motor cortex, 0.066–0.07 VGCs/cell in the striatum, 0.102–0.138 VGCs/cell in the thalamus, and 0.010–0.017 VGCs/cell in the cerebellum, an 11- and 5-fold increase compared with the 3E10 vg dose in jugular- and carotid artery-injected animals, respectively, averaged across brain regions.

After establishing that both venous and arterial injections led to similar AAV-PHP.B transduction in the brain, we next investigated potential differences between the two in the liver. We compared AAV-PHP.B transduction in mouse brain (all regions above averaged together) with that in the liver in mice injected at a dose of 1E11 VGs (Figure S2). A two-way ANOVA statistical analysis with tissue type and injection route as the independent variables and VGC numbers as the dependent variable detected significant differences in the total number of VGCs between injection route [$F(1,8) = 12.95$, $p < 0.01$], a non-significant trend between tissue type [$F(1,8) = 4.58$, $p = 0.06$], and a significant interaction between the two [$F(1,8) = 7.73$, $p < 0.05$]. Tukey's post hoc comparisons showed a 5-fold elevation in AAV-PHP.B transduction in liver following jugular vein administration (0.23 VGC/cell) compared with carotid artery administration (0.04 VGC/cell, $p < 0.01$). VGCs per cell in the liver following jugular vein injection was also significantly higher compared with those detected in the brain via both injection routes, whereas liver VGCs per cell post carotid artery administration was similar to that detected in the brain ($p > 0.05$). Together, the dose escalation study showed that we were able to significantly increase AAV-PHP.B transduction using either vascular approach, but that administration into the carotid artery reduces the characteristic "drain" of AAV in the liver compared with jugular vein administration.

Intrathecal Administration of AAV-PHP.B Leads to Superior Transduction in the Rhesus Macaque Cortex and Spinal Cord Compared with Intra-carotid Administration

Given the large interest in using recombinant viral vectors to translate studies conducted in rodents into human patients for myriad brain diseases, we next investigated the utility of AAV-PHP.B to deliver genes throughout the CNS in a larger-animal model. Naive 1- to 2-year-old juvenile rhesus macaques (n = 2 per group) received single infusions of AAV-PHP.B-EGFP into the right internal carotid artery or the cisterna magna at a dose of 2E12 VGs (1E12 VG/kg) delivered in a 2-mL volume, a dose that was comparable with the low dose used in our mouse studies described here (1.5E12 VG/kg). All non-human primates (NHPs) on study were weighed and pre-screened for anti-AAV9 neutralizing antibody titers, and only those that were negative (<1:5) were placed on study. See Table 1 for NHP group and AAV-PHP.B dose information and Table 2 for pre- and post-surgical body weight and pre- and post-surgical neutralizing antibody data. Animals were monitored daily by veterinary and laboratory staff, and rated weekly using our NHP neurological scale[53] to investigate the safety of AAV-PHP.B in NHPs. Animals were euthanized 3 weeks post-surgery, and this post-surgical interval was chosen to prevent potential toxicity stemming from the EGFP transgene. At necropsy, tissue was collected from several bilateral cortical and sub-cortical brain regions; cervical, thoracic, and lumbar spinal cord sections; and peripheral tissues including the liver, spleen, kidney, and gastrocnemius muscle. Transduction efficiencies between administration routes were visualized by using IF staining for EGFP to characterize biodistribution of AAV.PHP.B throughout the macaque CNS, and double-IF labeling was used to identify neuronal (NeuN$^+$), astrocytic (GFAP$^+$), microglia (Iba1$^+$), oligodendrocyte (Olig2$^+$), and vascular endothelial (CD31$^+$) cellular phenotypes. qPCR analysis of VGC number was used to statistically compare transduction efficiencies between

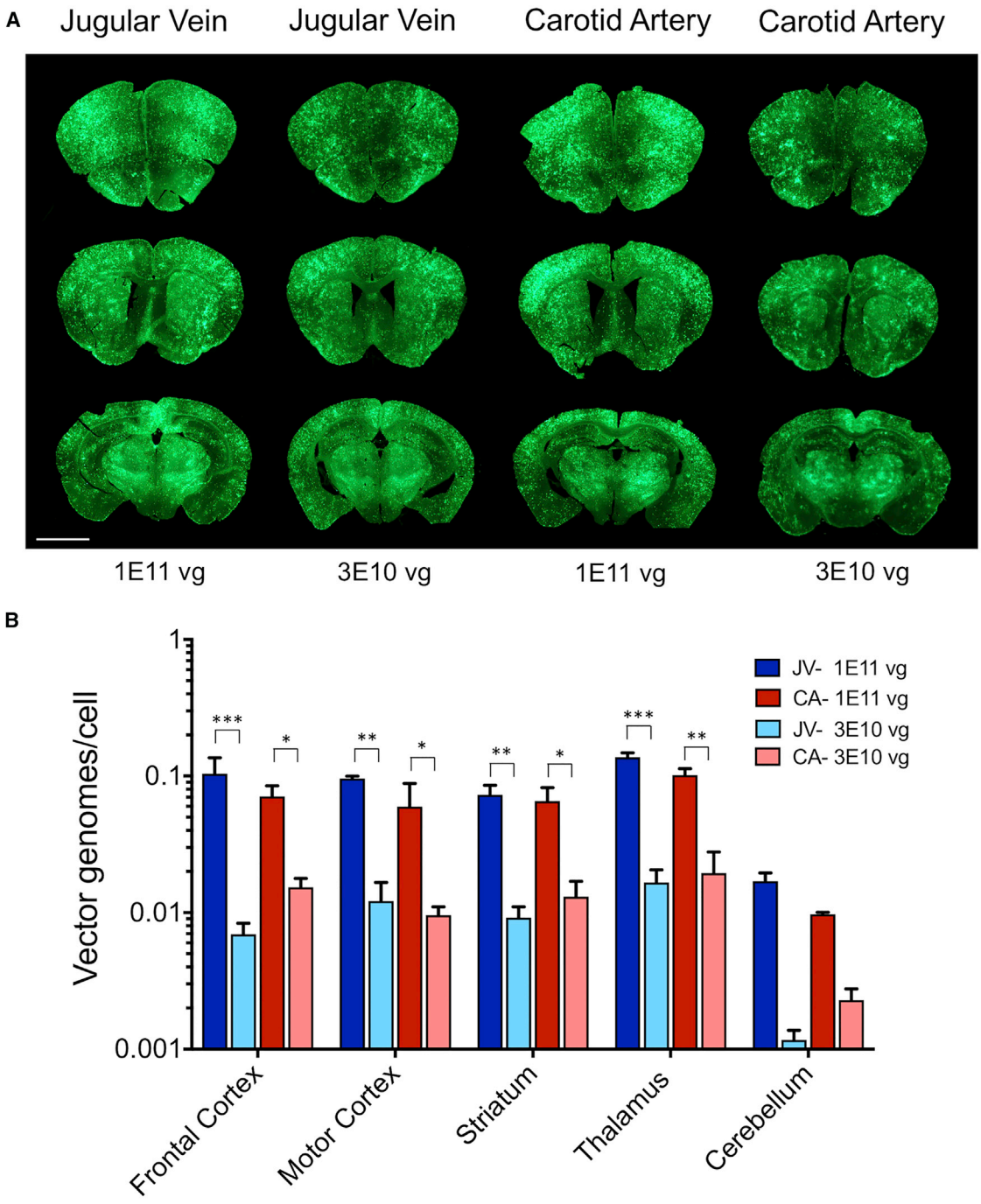

Figure 3. Dose Escalation of AAV-PHP.B in the Mouse Brain following Intravenous and Intra-arterial Delivery

(A) Representative EGFP$^+$ coronal brain images throughout the mouse brain comparing two doses of AAV-PHP.B injected into either the jugular vein rostral-to-caudal extent or carotid artery. EGFP$^+$ images were taken with a ×4 objective and montaged together. Photomicrographs show an increase in EGFP$^+$ staining throughout the mouse brain in animals injected at a dose of 1E11 VGs compared with 3E10 VGs following both routes of administration (n = 5 mice imaged per group). Scale bar represents 2 mm. (B) Dose escalation was confirmed with VGC qPCR analysis of five brain regions and two administration routes (presented as mean ± SEM vector genomes per cell), showing significantly higher AAV-PHP.B VGCs per cell in mice injected with 1E11 VGs compared with 3E10 VGs for all brain regions except for the cerebellum, regardless of vascular injection route ($p < 0.05$, n = 3 mice per group). *$p < 0.05$, **$p < 0.01$, ***$p < 0.001$.

Table 2. Neutralizing Antibody and Body Weight Analysis

Animal No.	Route of Administration	Pre-surgical Nab Screening	Necropsy Nab Analysis	Pre-surgical Body Weight (kg)	Necropsy Body Weight (kg)
CA1	internal carotid artery	<1:5	1:67	2.25	2.31
CA2	internal carotid artery	<1:5	1:2,183	1.5	1.8
CM1	cisternal magna	<1:5	1:657	2.15	2.17
CM2	cisterna magna	<1:5	1:2,396	2.1	2.03

All animals on study were weighed and pre-screened for anti-AAV9 neutralizing antibody titers, and only those that were negative (<1:5) were placed on study. Neutralizing antibody titers and body weight were also assayed at necropsy, 3 weeks post-surgery. CA, intra-carotid artery-injected animal; CM, intra-cisterna magna-injected animal; Nab, neutralizing antibody.

the two injection routes in brain, spinal cord, and peripheral tissue samples, similar to the mouse biodistribution studies reported here.

We detected EGFP-positive neuronal bodies (Figure 4, white chevrons), dendrites, and axons, as well as glia (Figure 4, yellow chevrons) and their processes, in several cortical and sub-cortical regions of injected rhesus macaques using double-labeled IF staining (EGFP and Hoechst) of coronal tissue sections; examples shown in Figure 4 are from the dorsal prefrontal cortex (Figures 4A–4D), orbitofrontal cortex (Figure 4E–4H), dorsal premotor cortex (Figures 4I–4L), superior temporal cortex (Figures 4M–4P), and putamen (Figures 4Q–4T). We saw a clear difference between injection routes in cortical regions, with the intrathecally injected animals showing a much higher density of positive cells throughout all cortical layers (Figure 4, left columns) compared with animals injected into the carotid artery (Figure 4, right columns), where cells were much sparser. Transduced neurons in the cortex were a mix of large spiny pyramidal neurons with dense dendritic branching and long axons containing numerous varicosities and smaller non-spiny neurons containing abundant shorter projections. In addition, $EGFP^+$ glia were detected (Figure 4, yellow chevrons). In both administration routes, AAV-PHP.B-transduced neurons were also observed in low numbers in several sub-cortical regions with an example shown here from the putamen, where we noted transduced neurons having the morphology of medium spiny neurons (Figures 4Q–4T, white chevrons). Figure S4 contains photomicrographs of additional cortical and subcortical regions of transduction (both delivery routes) taken at high magnification with a confocal microscope. Lumbar spinal cord from animals in both injection groups showed EGFP expression, with particularly high transduction in cells of the anterior horn in both groups (Figures 4U–4X), as well as numerous $EGFP^+$ fibers in ventral white matter columns in cisterna magna-injected animals (Figures 4U and 4V), likely reflecting the long axonal projections of the corticospinal tracts stemming from transduced cortical cells. Cell-type specificity in coronal NHP brain sections was verified with antibodies against EGFP and either NeuN, GFAP, Iba1, Olig2, or CD31. We found numerous examples of $EGFP^+$/$NeuN^+$ neurons (Figures 5A–5F, white arrowheads), $EGFP^+$/$GFAP^+$ astrocytes (Figures 5G–5L, white arrowheads), and $EGFP^+$/$CD31^+$ vascular endothelial cells (Figures 5M–5R), but no examples of $EGFP^+$/$Iba1^+$ microglia in any brain region examined (data not shown), similar to our findings in mice. We detected only very sparse $EGFP^+$/$Olig2^+$ cells in macaques infused into the cisterna magna and no examples of transduced oligodendrocytes in intravascularly infused animals (data not shown). Examples of double-labeled cells shown in Figure 5 are all from the motor cortex; however, similar expression patterns were seen throughout the brain.

VGC number between left and right hemispheres for each brain region analyzed was non-significant, and therefore data from each hemisphere was averaged for further statistical analyses ($p > 0.05$ for each brain region and dose). Intrathecal administration into the CSF led to higher AAV-PHP.B transduction compared with vascular delivery, with VGCs per cell ranging from 0.004 to 0.660 in the intra-cisterna magna-infused group compared with 0.0002–0.01 in the intra-carotid artery-infused group, an averaged 53-fold difference across all brain regions (Figure 6A). Planned t tests comparing the two injection groups revealed significantly higher VGCs in intrathecally injected animals in the orbitofrontal cortex [$t(2) = 6.33$, $p = 0.024$], dorsal pre-motor cortex [$t(2) = 29.57$, $p = 0.001$], superior temporal cortex [$t(2) = 8.62$, $p = 0.013$], and cerebellar cortex [$t(2) = 6.54$, $p = 0.023$], with a trend found in the hypothalamus [$t(2) = 4.02$, $p = 0.057$]. AAV-PHP.B transduction in the cervical and thoracic spinal cord was higher compared with that seen across the majority of brain regions, regardless of delivery method. Transduction ranged from 0.305 to 1.317 VGCs/cell in intrathecally injected monkeys and 0.002 to 0.034 VGCs/cell in intravascularly injected animals (Figure 6B), with no statistically significant differences found between the two injection routes ($p > 0.05$ for each analysis).

EGFP (transduced cells) and Hoechst (total cells) cell counts were performed on a small subset of transduced brain regions, including two cortical brain regions (orbitofrontal and dorsal premotor cortices) and one subcortical area (putamen), to assess the percent EGFP transduction (number of $EGFP^+$ cells/number of $Hoechst^+$ cells) in these brain regions (Figure 6C). EGFP cell counts were consistent with the VGC data, with a significantly higher percent of EGFP transduction found in the cortical regions in cisterna magna-infused monkeys (mean 0.9% transduction each in orbitofrontal and dorsal premotor cortices) versus carotid artery-infused monkeys (mean 0.04% transduction each in orbitofrontal and dorsal premotor cortices), and no differences were found in the putamen (mean 0.03% transduction in cisterna magna-infused animals and 0.07% transduction in carotid artery-infused animals). Planned t tests comparing the two injection groups confirmed significantly higher percent EGFP transduction in intrathecally injected animals in the orbitofrontal cortex [$t(6) = 4.88$, $p = 0.003$] and dorsal pre-motor

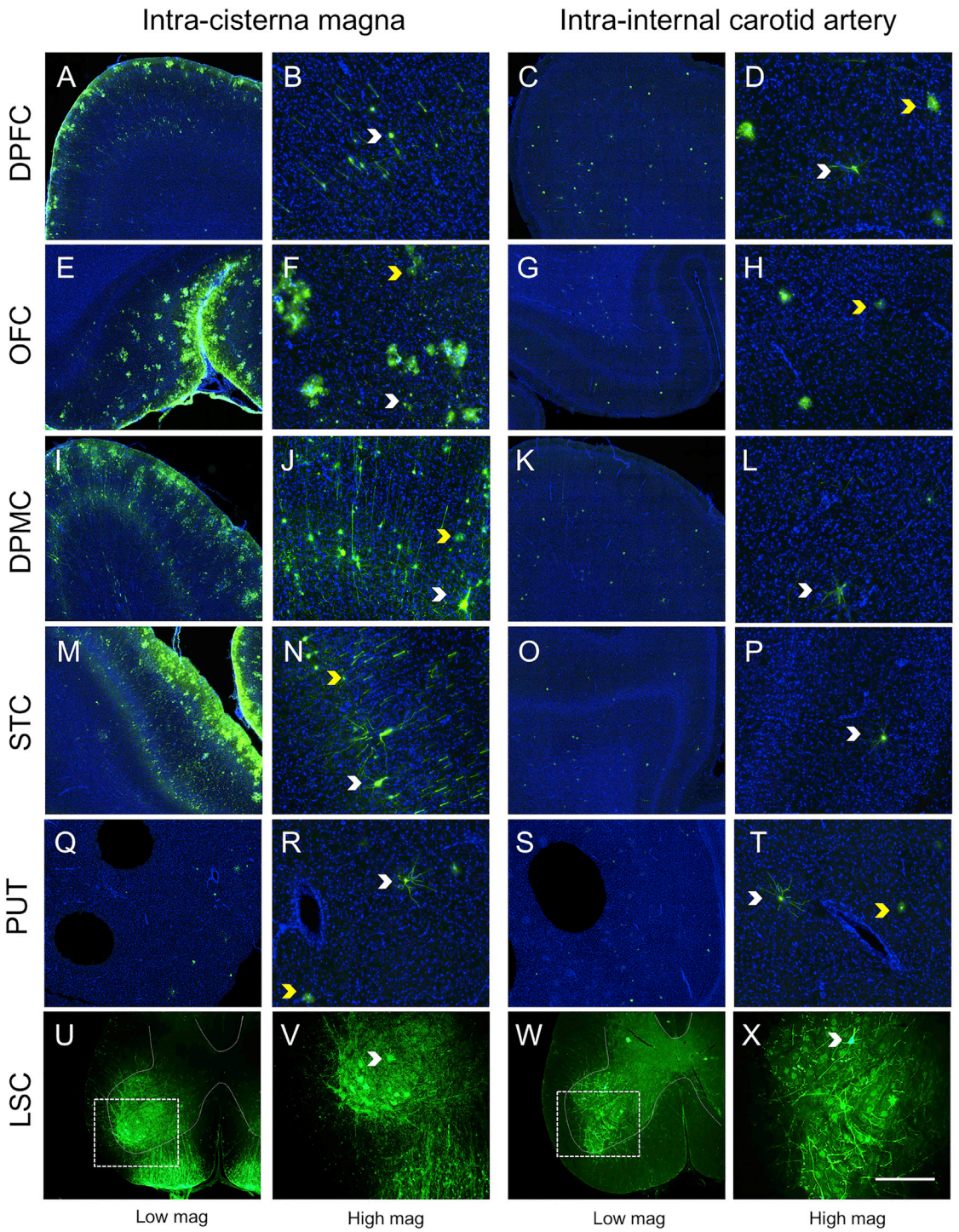

Figure 4. AAV-PHP.B Transduction in the Rhesus Macaque Brain and Spinal Cord following Intrathecal or Intravascular Administration

Double-labeled ($EGFP^+$/$Hoechst^+$) immunofluorescent coronal brain sections from rhesus macaques injected into either the cisterna magna (left panel, A–V) or the internal carotid artery (right panel, C–X); n = 2 monkeys imaged per administration route. Animals injected into the cisterna magna showed several more transduced neurons (white chevrons) and glia (yellow chevrons) throughout the cortex compared with those injected into the carotid artery, with GFP^+ cells observed in both deep and superficial cortical layers. Robust EGFP expression was also detected in anterior horn cells in the lumbar spinal cord (white chevrons, U–X), regardless of the

(legend continued on next page)

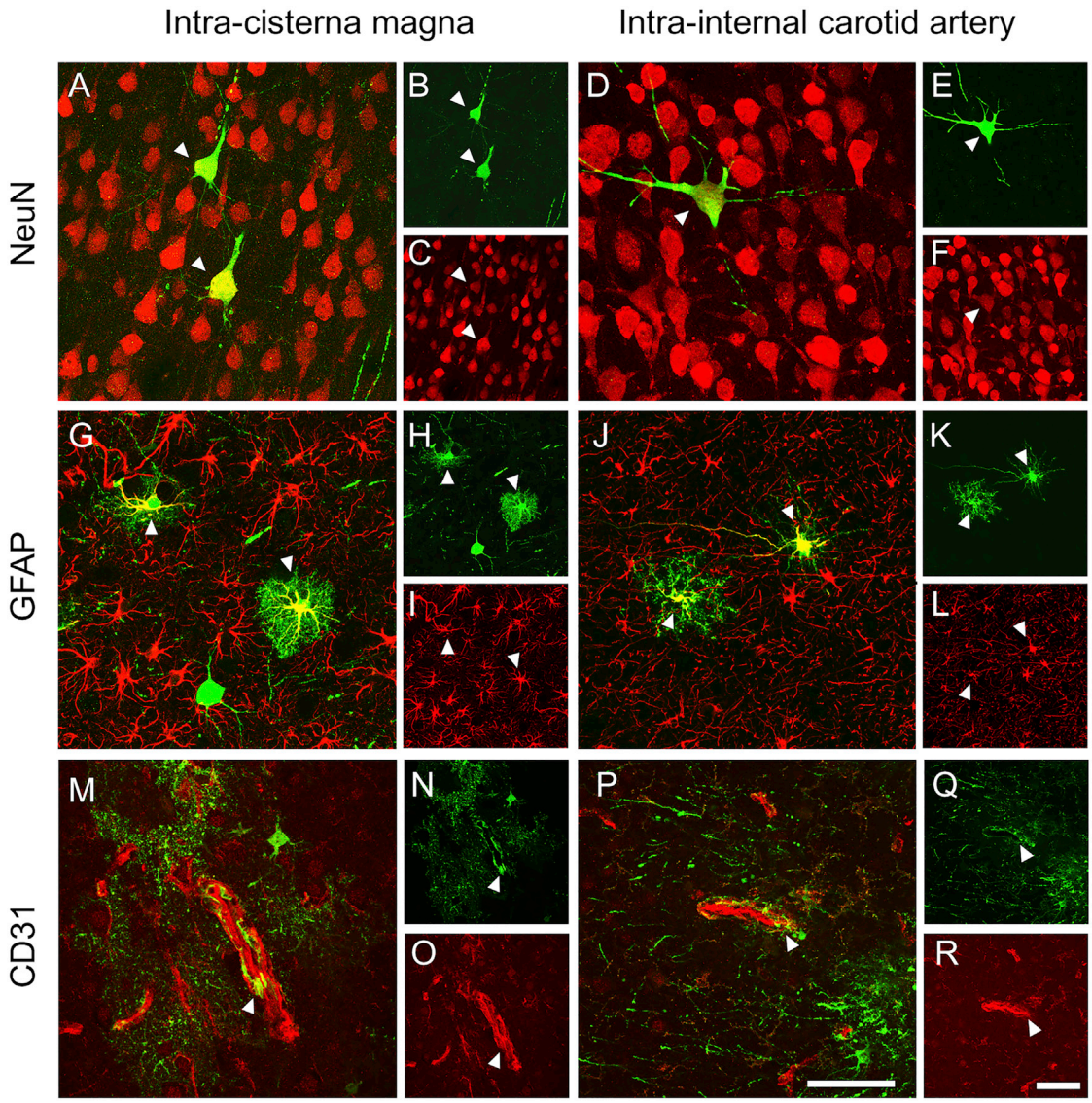

Figure 5. AAV-PHP.B Shows Tropism for Neurons, Astrocytes, and Vascular Endothelial Cells in the Rhesus Macaque Brain following Intrathecal or Intravascular Administration

Confocal microscope images (×63 objective) show double labeling of green GFP$^+$ cells and either red NeuN$^+$ neurons (A–F), GFAP$^+$ astrocytes (G–L), or CD31$^+$ vascular endothelial cells (M–R) in the motor cortex following AAV-PHP.B injection into the cisterna magna (left panel) or the internal carotid artery (right panel). Transduced neurons, astrocytes, and vascular endothelial cells are indicated with arrowheads. Scale bars represent 50 μm (P and R); n = 2 monkeys imaged per administration route.

cortex [t(6) = 4.94, p = 0.003], but not the putamen [t(6) = 0.229, p = 0.826], compared with intra-carotid-infused animals.

Unlike our findings in mice, AAV-PHP.B transduction in the liver (1.468–5.603 VGCs/cell) and spleen (0.586–4.826 VGCs/cell) was higher compared with transduction in the brain regardless of injection modality (Figure 6D). Transduction in the kidney (0.015–0.074 VGCs/cell) and gastrocnemius muscle (0.011–0.052 VGCs/cell) was lower compared with the liver and spleen, but this difference was not statistically significant. Moreover, we found no statistically significant differences between the two injection routes for all peripheral tissues (p > 0.05 for each analysis).

administration route; however, more fibers were noted in the descending corticospinal tracts in NHPs injected into the cisterna manga. (X) Scale bar represents 500 μm for all low-magnification photomicrographs (first and third columns) and 200 μm for all high-magnification photomicrographs (second and fourth columns). DPFC, dorsolateral prefrontal cortex; DPMC, dorsal premotor cortex; LSC, lumbar spinal cord; OFC, orbitofrontal cortex; PUT, putamen; STC, superior temporal cortex.

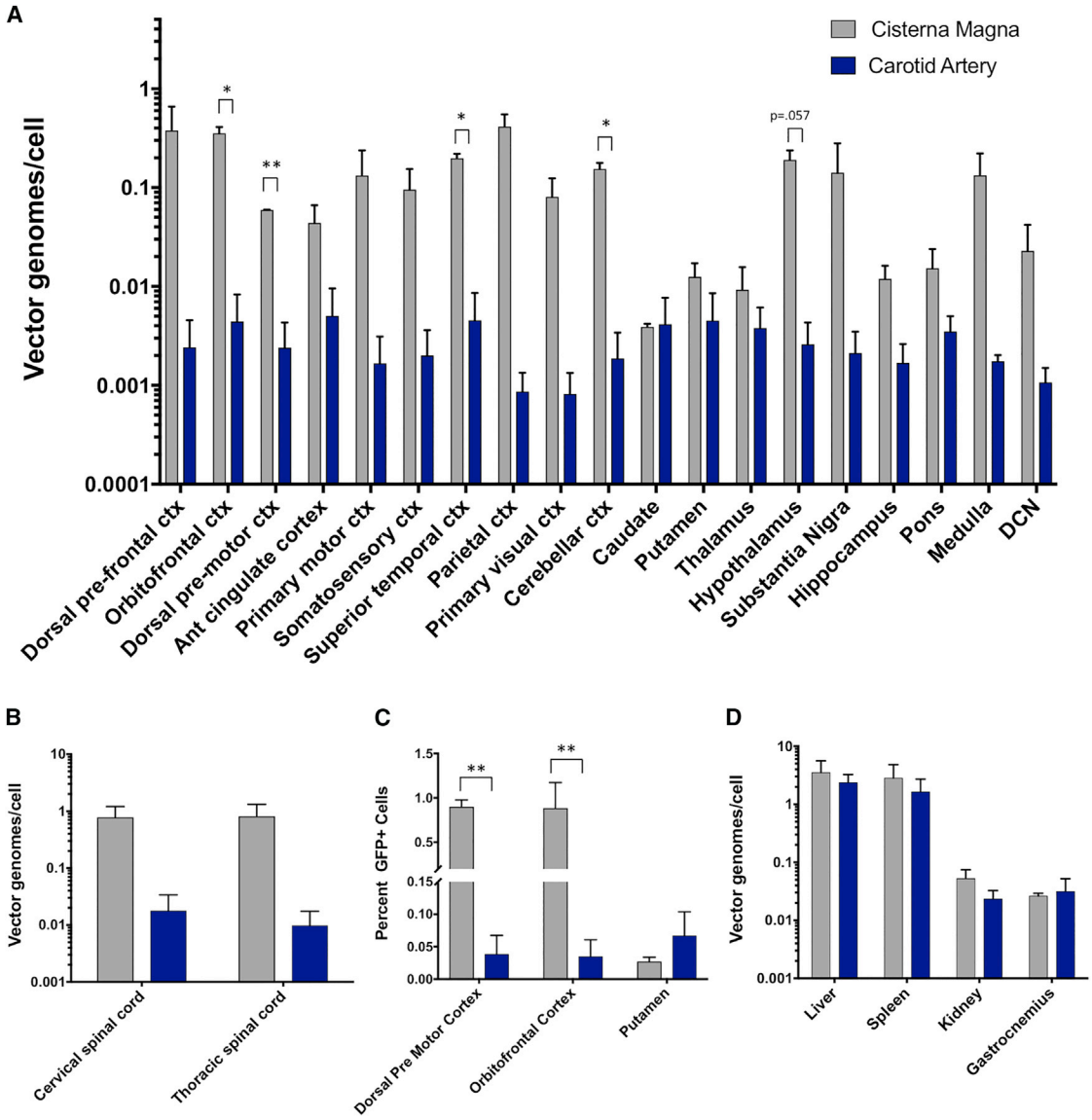

Figure 6. Cisterna Magna Administration of AAV-PHP.B Yields Greater Transduction Than Carotid Artery Administration in NHP CNS

Vector genome copy analysis via qPCR demonstrates that although both delivery strategies resulted in transduction in the rhesus macaque brain (A) and spinal cord (B), cisterna magna infusions led to significantly higher numbers of vector genomes per cell in multiple cortical regions including frontal, motor, temporal, and cerebellar cortices, compared with carotid artery administration (presented as mean ± SEM vector genomes per cell, $p < 0.05$ for each structure). Similarly, the percent of EGFP expression ($EGFP^+$ cells/$Hoechst^+$ cells) was significantly higher in the orbitofrontal and dorsal premotor cortex of animals injected into the cisterna magna compared with the carotid artery (C, $p < 0.01$ for both cortical regions). No differences in percent EGFP expression were detected in the putamen (C, $p > 0.05$). Additionally, we found no differences in AAV-PHP.B transduction in the liver, spleen, kidney, or gastrocnemius muscle between delivery methods (D, $p < 0.05$). n = 2 monkeys evaluated per administration route. Ctx, cortex; DCN, deep cerebellar nuclei. *$p < 0.05$, **$p < 0.01$.

Safety and Tolerability Measurements following AAV-PHP.B Administration in Rhesus Macaques

Several in-life and post mortem measurements of safety and tolerability were assessed in the four macaques that received AAV-PHP.B administration. Body weight assessed prior to surgery and necropsy showed that three out of the four animals gained weight from baseline to necropsy, and one animal who received injection into the cisterna magna lost 0.07 kg, equivalent to 3% body weight (Table 2). Blinded to the animals' treatment groups, we evaluated each animal at baseline and weekly thereafter until necropsy using our NHP-specific neurological rating scale,[53] which assesses home cage horizontal and vertical gaze, posture, balance, forelimb and hindlimb strength, startle response, bradykinesia, dystonia, chorea, ataxia, and dysmetria. We found that all animals in each group had normal behavior

at baseline and at each week post-surgery, with no development of clinical neurological symptoms throughout the study. In the two animals who received injection through the internal carotid artery, we noted temporary miosis (pupil restriction) and ptosis (eyelid droop) on the injected side, reminiscent of Horner's syndrome, that persisted for 7 days post injection and resolved with no further complications. This most likely resulted from small perturbations to the surrounding tissue in the neck while the internal carotid artery was isolated during surgery rather than from the injectate.

Qualitative analysis of coronal sections throughout the brain stained with antibodies to NeuN, GFAP, and Iba1 showed no indication of neuronal loss, astrogliosis, or microgliosis, respectively, throughout the rostral-to-caudal extent of the brain. The Oregon National Primate Research Center (ONPRC) Pathology Services report from necropsy found no gross lesions of the respiratory, cardiovascular, hemopoietic, gastrointestinal, genitourinary, endocrine, or musculoskeletal systems, as well as no damage to the liver and pancreas in three of four monkeys receiving injections of AAV-PHP.B (both cisterna magna-infused animals and one carotid artery-infused animal). Both animals receiving vascular injections showed mild scar tissue surrounding the right carotid artery caudal to the bifurcation of the internal and external arteries. One of the two carotid artery-infused animals, CA2, showed evidence of mildly enlarged mesenteric lymph nodes and mild diffuse fibrosis in the liver upon gross examination. Further microscopic evaluation of H&E-stained liver tissue in this animal showed multifocal portal lymphocytic and neutrophilic infiltrates and mild subcapsular lymphatic dilation, hepatocellular anisokaryosis with increased numbers of binucleated and multinucleated hepatocytes, and mild evidence of hepatocellular degeneration.

Neutralizing antibody analysis was performed on serum collected from all animals at baseline and necropsy using a cell-based assay. Results indicated an increase in anti-AAV9 neutralizing antibody titers from baseline (<1:5 in all animals) in all four treated animals, with no clear pattern detected between animals in the two different groups (Table 2). CA1 and CA2 had antibody titers of 1:67 and 1:2,183 at necropsy, respectively, whereas CM1 and CM2 had titers of 1:675 and 1:2,396, respectively.

DISCUSSION

The ability to deliver therapeutic agents throughout the CNS to treat neurological disorders characterized by global neuropathology remains a difficult, but not insurmountable, hurdle. Significant strides have been made in the field of gene therapy to develop and characterize new viral vector serotypes; however, further improvement is still needed to maximize the efficiency and spread of these vectors throughout the brain and spinal cord. To aid in these efforts, the current study was undertaken to directly compare the biodistribution and safety of the newly designed AAV9 capsid variant, AAV-PHP.B, throughout the CNS and peripheral tissues of mice and NHPs using several clinically viable surgical delivery modalities, including intravascular and intra-CSF routes of administration. The four delivery routes investigated here were carefully chosen to allow us to answer several key questions. First, we sought to determine a superior administration route of AAV-PHP.B when directly comparing two intravascular (intra-jugular or intra-carotid) and two intra-CSF (intra-cerebroventricular and intra-cisterna magna) delivery strategies in mice that could be feasibly scaled up in non-human and human primates. Second, we evaluated whether any of the unilateral administration routes of AAV-PHP.B we employed resulted in a higher transduction efficiency in the injected hemisphere, an obvious detriment to a brain-wide gene therapy strategy. Third, we investigated the direct translatability of our findings in mice to the much larger CNS of the rhesus macaque using identical delivery modalities as a precursor to future pre-clinical gene therapy studies using AAV-PHP.B in both mouse and NHP models of neurodegenerative diseases established in our laboratory, including Huntington's and Batten diseases.

Interestingly, we found largely equal transduction efficiency of AAV-PHP.B throughout several regions of the mouse brain when directly comparing the four administration routes, with no single injection route emerging as clearly superior. Lateral ventricle administration led to higher transduction in the striatum and thalamus compared with the other routes; however, significantly elevated transduction in the striatum was seen in one hemisphere only, on the same side as the injection, which is perhaps not surprising given their close proximity. Although this may be perceived as a limitation to this delivery strategy, particularly where hemispheric differences could complicate dosing and provide only partial symptom relief, bilateral ventricular infusions may alleviate this problem and result in a more uniform distribution. Although the primate circle of Willis forms a closed circuit, in mice and other rodents the circle is not complete, and agents injected into one artery only typically show a unilateral pattern of biodistribution in brain.[54,55] Therefore, we anticipated a potential hemispheric discrepancy in mice receiving intra-carotid artery infusions compared with intra-jugular infused mice that we did not detect. Given that AAV persistence in blood has been demonstrated for up to 48 hours following tail vein infusion, with AAV9 persisting significantly longer than other AAV serotypes,[56–58] it is possible that AAV-PHP.B functions similarly and remains in circulation long enough to even out any initial hemispheric differences from a unilateral injection or perceived potential "first-pass" benefit from a carotid artery administration. Although there were no differences in AAV-PHP.B-mediated brain transduction between jugular- and carotid-infused mice, we found a significant 5-fold reduction in liver transduction following carotid artery administration, corroborating recent evidence by Morabito et al.,[59] who recently documented similar findings in a mouse model of synucleinopathy. The reduction in peripheral tissue AAV-PHP.B transduction may be an important advantage of the carotid artery infusion strategy, particularly given the high tropism of most AAVs to liver, potential off-target effects of transducing this organ, and the recent demonstration of AAV-related immunogenicity and elevated liver enzymes at very high systemic titers in large-animal models.[60,61]

At the highest dose of AAV-PHP.B evaluated in mice (1E11 VGs), we achieved transduction levels in the brain of approximately

0.10 VGC/cell, averaged across brain regions. A practical way to interpret these data is that we transduced, on average, 1 out of every 10 cells in the mouse brain. Compared with the transduction efficiency in brain originally reported by Deverman et al.,[41] our findings at the same dose (1E11 VGs) were approximately 10-fold lower. Potential reasons for this discrepancy may be because of several factors. First, although both studies used a single-stranded AAV-PHP.B vector at the same dose, viral vector preps for each study were made at different institutions (California Institute of Technology [Cal Tech] versus Oregon Health and Science University [OHSU]), and small differences in production, purification, and tittering methods may result in prep-to-prep variability. Additionally, VGCs in Deverman et al.'s[41] study were determined using PCR primers that bind to the Woodchuck hepatitis virus post-transcriptional regulatory element (WPRE) in the vector, whereas we used primers that bind to the CAG promoter sequence. Both laboratories normalized to mouse genomes using primers specific to the mouse glucagon gene. The reasoning behind using different primer sets between labs was the discovery that the WPRE primer used by Deverman et al.[41] also amplifies a region of the rhesus macaque genome. So that we could keep methods consistent between our mouse and NHP analyses, priming the CAG promoter was more desirable. Lastly, while we both investigated intravascular routes of administration, there may be inherent differences in how AAV-PHP.B reaches the brain following a retro-orbital infusion compared with jugular vein and carotid artery infusions. A similar finding was recently reported by Gruntman et al.,[62] who found higher transduction in mouse brain following retro-orbital administration of AAV9 compared with facial vein infusion. It is interesting to speculate whether a retro-orbital infusion of AAV-PHP.B in rodents results in different diffusion properties into brain compared with other venous routes of administration, particularly at high volumes or rates of administration. For example, the retro-orbital sinus drains intracranially into the cavernous sinus and basilar plexus, in addition to draining into the external jugular vein.[62] This highlights the larger point of the importance in the selection of administration route when comparing data between studies in the same species, comparing across different species, and importantly, when scaling gene therapy studies up in species that do not share the same anatomy. Although retro-orbital sinus and tail vein are the most commonly used routes of venous administration in rodents likely because of ease of a less invasive injection, these delivery routes may not be as directly translatable in terms of working up a pre-clinical gene therapy strategy from mouse to primate.

In order to scale our findings in mice to a larger and more clinically translatable animal model, we evaluated biodistribution of AAV-PHP.B in juvenile rhesus macaques, comparing one intravascular and one intra-CSF approach. Although both jugular vein and carotid artery delivery modalities in mice resulted in a similar transduction profile in the brain, the 5-fold higher elevation of AAV-PHP.B VGCs in the liver of jugular vein-infused animals precipitated our choice of an intra-carotid artery delivery strategy in the NHP study. Additionally, because lateral ventricle injections led to increased transduction in the striata of the injected hemisphere compared with the contralateral hemisphere in mice, we chose the cisterna magna for our intra-CSF delivery site in NHPs to increase the chance for a more uniform distribution throughout the CNS. Although the more common route of intrathecal administration in clinical studies has been via lumbar puncture, likely because it is less invasive compared with intra-cerebroventricular or intra-cisterna magna infusions, recent evidence from Hinderer et al.[63] demonstrates a 100-fold more efficient gene transfer of AAV9 throughout the NHP brain when delivered by intra-cisterna magna infusion compared with intra-lumbar infusion. The two delivery modalities chosen for the NHP study are both considered to be relatively non-invasive compared with intraparenchymal infusion and, therefore, desirable for translating gene therapy strategies from mice to large-animal models and ultimately into human patients. The dose of AAV-PHP.B used in the NHP study (1.5E12 VG/kg) was comparable with the low dose used in our mouse studies (1.5E12 VG/kg). Although the rodent studies presented here showed largely equal transduction of AAV-PHP.B regardless of injection route, the intra-CSF delivery into the cisterna magna in monkeys resulted in a substantial 50-fold higher transduction efficiency throughout the CNS compared with intra-carotid artery delivery, with regions of the frontal, motor, temporal, parietal, visual, and cerebellar cortices showing the highest levels of transduction. Cortical areas showed the highest transduction; however, we did detect a very low level of transduction in several subcortical areas including the caudate, putamen, hypothalamus, substantia nigra, and medulla. The transduction level achieved in NHPs was higher than seen in mice via cisterna magna infusion (~10-fold higher throughout brain), but lower than seen in mice via the intra-carotid route (~10-fold lower throughout brain). We found that AAV-PHP.B transduces spinal cord neurons of the anterior horn exceptionally well following both administration routes, with higher transduction efficiency seen following cisterna magna delivery.

Our data with AAV-PHP.B in NHPs corroborate findings by several other labs that have showed higher transduction of AAV9 in brain and spinal cord following intra-thecal delivery compared to intravascular administration.[35,45,64–69] However, several of these reports demonstrate that the intra-CSF delivery of AAV-PHP.B resulted in significantly fewer transduced cells in peripheral organs, whereas we found that intra-CSF and intra-carotid artery administration of AAV-PHP.B resulted in equal transduction in all of the peripheral organs we measured. Why this discrepancy exists is unclear. However, several differences between our study and these previous reports exist, including: (1) the slower intra-CSF infusion rate used in our study (100 μL/min) compared with some of the other studies, which could result in prolonged drainage of AAV-PHP.B into the bloodstream; (2) species and age differences because many of these studies assessed AAV transduction in adult cynomolgus macaques versus the juvenile rhesus macaques evaluated here; and (3) vector construct differences including our use of a single-stranded vector versus a double-stranded, self-complementary vector used in many of the other studies. There may also simply be differences between AAV9 and AAV-PHP.B capsids that result in the difference in

transduction of peripheral tissues following an intra-CSF infusion. That being said, our results in NHPs showed highest peripheral transduction of AAV-PHP.B in the liver and spleen compared with other peripheral organs including the kidney and gastrocnemius muscle following intrathecal or intravascular infusion, which has also been reported for AAV9.[35,65]

Recently, Matsuzaki et al.[69] and Hordeaux et al.[70] reported that AAV-PHP.B does not enhance transduction in the marmoset and rhesus macaque brain, respectively, compared with AAV9. Moreover, Hordeaux et al.[70] concluded that the neurotropic properties of AAV-PHP.B are limited to the C57BL/6J mouse, the species in which it was developed. Although we cannot comment on which of these two vectors performs best in the NHP because we did not directly compare AAV9 with AAV-PHP.B, we report here that the neurotropic properties of AAV-PHP.B are not limited to the C57BL/6J mouse, because we found transduction of neurons and astrocytes in the brain and spinal cord of the rhesus macaques, even at a 20-fold lower dose than what was used by Hordeaux et al.[70] as their low dose (1E12 VG/kg compared with 2E13 VG/kg). However, it does appear that transduction of AAV-PHP.B in the NHP brain is highly dependent on the delivery route, because we noted very low transduction of AAV-PHP.B following the intra-carotid approach compared with the intra-CSF approach. A recent follow-up publication by Hordeaux et al.[70] sheds light on our findings, because they demonstrated via an eloquent series of studies that the G glycosylphosphatidylinositol-linked protein, lymphocyte antigen 6 complex, locus A (LY6A), acts as a co-receptor and transports AAV-PHP.B across the BBB in mice when the virus is injected intravascularly.[71] Interestingly, although several mouse strains, including the C57BL/6J strain used here, express LY6A, primates lack an LY6A homolog.[72] The higher transduction observed in the cortex, cerebellum, and spinal cord of the cisterna magna-infused animals in our study makes sense given that the virus does not have to penetrate the BBB via this route of administration and likely accesses neurons and glia in the brain first via traveling through the glymphatic system and then by passing through extracellular space in these brain regions. We speculate that AAV-PHP.B is then able to transduce neurons and glia via binding to cell surface receptors already identified for AAV9, including N-linked galactose[73] and the universal AAV receptor, AAVR.[73,74]

Another difference that exists between our study and that of Hordeaux et al.[70] is that we evaluated juvenile rhesus macaques (age 1–2 years), whereas their study used adults (age 4), and inherent differences may exist in how AAV-PHP.B transduces juvenile versus adult rhesus macaque brain. Despite differences in brain and spinal cord transduction, our data corroborate those of Hordeaux et al.[70] with respect to our findings of higher AAV-PHP.B transduction found in liver and spleen compared with brain. At a much higher dose of AAV-PHP.B (7.5E13 VG/kg), Hordeaux et al.[70] reported acute toxicity in NHP characterized by activation of innate immunity and elevated liver enzymes that necessitated euthanasia of their study animal at day 5 post-infusion. In the current study, we found mild histological abnormalities in the liver of one carotid artery-infused animal, but found no abnormalities in CNS or any peripheral tissues in the second carotid artery-infused animal or in either of the two cisterna magna-infused animals. The cause of these findings in animal CA2 are uncertain, particularly because they do not correlate with a higher AAV-PHP.B VGC expression in the liver of this animal compared with the other three study animals. The mild histological abnormalities found in this animal's liver did not cause any phenotypic changes in the animal's temperament, food and water consumption, locomotor behavior, nor any negative changes in body weight throughout the study; however, the time to necropsy here was relatively short at 3 weeks post-surgery. Given the high tropism of both AAV9 and AAV-PHP.B for hepatocytes, it is advised that future studies utilizing these rAAVs should vigilantly monitor transduction profiles, enzyme levels, and potential signs of toxicity in this organ. The two carotid artery-infused animals showed temporary miosis and ptosis on the injected side that resolved after 1 week with no further complications. This most likely resulted from small perturbations to the neck tissue while isolating the carotid artery during surgery. This issue, although minor, can be circumvented in future studies by using remote catheterization of the internal carotid artery from the femoral artery under image guidance such as fluoroscopy.[42,43]

The set of studies presented here confirms a high tropism of AAV-PHP.B in wild-type C57BL/6J mice. Importantly, we also show that although AAV-PHP.B can successfully and equally express transgenes throughout the CNS of mice from four different intravascular and intra-CSF delivery modalities, when translated into the macaque, a large disparity exists, with the intra-cisterna magna route of administration showing clear superiority over the intra-carotid artery infusions. Due to volume limitations of infusing into CSF, it is more difficult to scale up AAV dosing using this route compared with an intravascular infusion. However, transduction efficiencies can be enhanced by using higher titer viral vector preparations, using double-stranded versus single-stranded viral vectors, and by reducing infusion rates.[75] Moreover, body position appears to play an important role in transduction efficiency, because it has been shown that maintaining NHPs in the Trendelenburg position (supine with the feet elevated above the head) for 10 min post-intrathecal infusion significantly enhances AAV9-mediated brain transduction.[35]

Taken together, these data demonstrate the use of AAV-PHP.B for the delivery of transgenes throughout the CNS of mice and in the cortex and spinal cord of rhesus macaques. Given the disparity in transduction profiles in the macaques using the different delivery routes, we highly recommend an intra-CSF delivery route when using AAV-PHP.B in primates. This vector may be a good clinical candidate to deliver transgenes for a variety of neurological disorders that would benefit from gene expression to the cortex, cerebellum, and spinal cord, including lysosomal storage diseases, RS, AD, multiple sclerosis, amyotrophic lateral sclerosis, and the various forms of ataxia. Careful studies are needed to directly compare the transduction efficiencies of AAV9 and AAV-PHP.B when administered into the CSF to address whether this new capsid variant shows enhanced

transduction compared with the gold standard, AAV9, which is now in pre-clinical and clinical development for a variety of CNS disorders. For diseases where substantial cortical and subcortical transduction is desired, such as Huntington's disease, the new AAV serotype 2 capsid variants, including AAV2.retro[76] and AAV2-HBKO,[77] which exhibit robust retrograde transport from the sight of injection, may be an attractive alternative to target multiple affected brain circuits versus a single brain region.

MATERIALS AND METHODS

Vector Preparation

pAAV-PHP.B plasmids were sent to Dr. McBride by Dr. Deverman under a material transfer agreement between OHSU and Cal Tech. rAAV vector was generated by a scalable co-transfection procedure in the OHSU/ONPRC Molecular Virology Support Core. Plasmids carrying the transgene cassette flanked by viral inverted terminal repeats (ITRs) (sspAAV-PHP.B-CAG-EGFP), a rep-cap expression construct encoding the sequence for the AAV-PHP.B serotype capsid, and a helper plasmid expressing adenoviral E2a, VA, and E4-orf6 were transfected into mammalian HEK293 producer cells. Viral lysates were treated with Benzonase to remove residual plasmid, and virus was purified over an Iodixanol step gradient. Gradient fractions containing intact virus, and excluding empty particles, were harvested, and the final virus preparation was buffer exchanged into Dulbecco's PBS (DPBS) + 5% glycerol + 35 mM NaCl. Quality control was performed to ensure purity by viral capsid protein evaluation by silver staining on SDS-PAGE. Viral titers were determined by qPCR of purified vector particles using a CAG primer-probe set: forward: 5′-CCATCGC TGCACAAAATAATTAAAA-3′, reverse: 5′-CCACGTTCTGCTTCA CTCTC-3′, probe: 5′-CCCCTCCCCACCCCCAATTTT-3′.

Animal Breeding and Husbandry

Mice

All mice (12- to 16-week-old male and female adults) were group housed with littermates under controlled conditions of temperature and light (12-hour light/dark cycle). Food and water were provided *ad libitum*. WT C57BL/6J were obtained from Jackson Laboratories (Bar Harbor, ME, USA) and bred in the vivarium at the ONPRC. Only F1 generation, adult mice were used in the current study. Mice were observed by trained veterinary technicians daily in their home cages, and body weights of all animals were recorded weekly.

Rhesus Macaques

Four male juvenile rhesus macaques of Indian origin that were bred at the ONPRC were used in the current study (age 1–2 years). All animals were pair housed on a 12-hour on/12-hour off lighting schedule with *ad libitum* access to food and water. Animals were fed standard primate chow twice daily and provided fruit and vegetable enrichment daily. Macaques were observed by trained veterinary technicians daily in their home cages, and body weights of all animals were recorded weekly. All experimental procedures were performed according to ONPRC and OHSU Institutional Animal Care and Use Committee- and Institutional Biosafety Committee-approved protocols.

Neutralizing Antibody Analyses

Whole blood was collected in Vacutainer Serum Collection Tubes (BD), and serum was collected following centrifugation at 2,500 rpm for 10 min and stored at −80°C until analysis. Initial neutralizing antibody screening assays were carried out in 96-well format with 5×10^4 CHO-Lec2 cells per well. Three dilutions of study participant serum (1:5, 1:20, 1:80) were pre-incubated with 1E+9 GCs of AAV9 reporter virus for 1 h at 37°C and then added to cells that have been infected with Adeno Helper virus. After 48 h, Promega Bright-Glo substrate was added to the cells, and luciferase expression was quantified using the Biotek Synergy Mx luminometer. For the final 50% infective dose (ID_{50}) assay, samples were tested for neutralizing antibodies starting at a 1:5 dilution, and serial 2-fold dilutions were made for a total of 11 dilutions. The neutralizing antibody titer at 50% inhibition of virus transduction was calculated based on the global fitting of the data obtained from each of 11 antibody dilutions using Gen 5 software. Both positive and negative monkey sera controls were included with each assay.

Surgery

Mice

Carotid artery. Animals were anesthetized with isoflurane, and the surgical site was shaved and prepared for incision with a betadine solution (10% povidone-iodine) followed by 70% ethanol. An incision was made along the animal's right neck to expose the carotid artery. Connective tissue covering the carotid artery was bluntly dissected, and the vagus nerve was dissected free from the carotid artery. A suture was tied tightly around the posterior portion of the carotid artery, and the second suture was placed loosely around the anterior portion with 5 mm between the sutures. A 25G needle bent at a 90-degree angle was used to make an opening in the artery. A 1.5 Fr catheter connected to a 250-μL Hamilton syringe was inserted several millimeters into the artery. A microvascular clamp was then placed around the artery to prevent leakage during infusion. The syringe was loaded into a Stoelting quintessential stereotaxic injector pump to control the infusion. Mice received 60 μL of diluted virus into the right carotid artery over the course of 3 min (diluted with sterile 1× PBS w/0.001% Pluronic F-68 to a final dose of 3E10 VGs or 1E11 VGs). Upon completion of the infusion, the top suture was tightened and the catheter was withdrawn. The incision was closed with 5-0 Polysorb dissolvable sutures (Covidien), and animals were placed in a cage to recover.

Jugular Vein. Mice were anesthetized with isoflurane, and the surgical site was shaved and prepared with a betadine solution (10% povidone-iodine) followed by 70% ethanol. An incision was made along the animal's right neck to expose the jugular vein. Forceps were used to grasp the pectoral muscle, and a 30G needle attached to a 100-μL Hamilton syringe was inserted through the pectoral muscle into the jugular vein. Mice were injected with 60 μL of diluted virus into the right jugular vein over the course of 3 min. The incision was sutured using 5-0 Polysorb dissolvable sutures (Covidien) and further secured using Vetbond (3M), and animals were placed in a cage to recover.

Lateral Ventricle. Mice were anesthetized with isoflurane and their scalps shaved before being mounted into a Kopf Model 900 stereotaxic apparatus. The scalp was prepared with Betadine followed by 70% ethanol, and an incision was made to expose the skull. Using bregma as a reference point, coordinates of anteroposterior (A-P): −0.5 and mediolateral (M-L): −1.0 were used to mark the skull so that a hole could be drilled with a Dremel tool. After re-centering at bregma, a 25-μL Hamilton syringe with a 30G blunt-tipped needle was slowly lowered into the coordinates A-P: −0.5, M-L: −1.0, and dorsoventral (D-V): −2.0 (left lateral ventricle). After a 3-min wait period, 15 μL of virus was infused at a rate of 0.5 μL/min (virus was diluted with sterile PBS to a final dose of 3E10 VGs). After completion of the infusion, the needle was left in place for 5 min before being slowly withdrawn out of the brain. The scalp was then sealed with Vetbond (3M), and animals were placed in a cage to recover.

Cisterna Magna. Mice were anesthetized with isoflurane, and the nape was shaved before mice were mounted in a stereotaxic apparatus with the front of the head tilted downward at a 30-degree angle. The surgical site was prepped with Betadine, and an incision was made from the base of the neck to lambda. Forceps were used to bluntly dissect the muscle apart and expose the dura mater overlying the cisterna magna. A 25-μL Hamilton syringe with a 33G needle that has a bevel angle of 25 degrees was loaded into the stereotaxic arm. The arm of the stereotaxic frame was placed at a 45-degree angle. The cisterna magna was visualized just ventral to the cerebellum, and the needle tip was advanced 0.75 mm past the dura into the cisternal space. 15 μL of virus was infused a rate of 0.5 μL/min (virus was diluted with sterile PBS to a final dose of 3E10 VGs). Following infusion, the needle was retracted, the incision was closed with Vetbond (3M), and animals were placed in a cage to recover.

Rhesus Macaques

Cisterna Magna. After positioning in lateral recumbency, sterile prep of the posterior neck was performed, and the head was held in flexion. A 22G, 3-inch spinal needle was inserted and stabilized in the cisterna magna, confirmed by back flow of cerebrospinal fluid. A 36-inch micro-extension line ending in a three-way stock cock was connected to the spinal needle, and a 1.5-mL sample of CSF was then obtained using a 3-mL syringe. The syringe was replaced with a sterile syringe containing 2.0 mL of viral vector infusate for a total dose of 2E12 VGs. The infusate was slowly delivered through the spinal needle into the cisterna magna over 20 min (100 μL/min). The needle was then flushed with 0.1 mL of the patient's CSF at the same rate and removed. Animals recovered on the operating room table until extubation; thereafter, they were returned to their home cage.

Carotid Artery. Positioning was in dorsal recumbency with sterile preparation and draping of the neck region. A 4-cm curvilinear incision was created along the lateral aspect of the neck extending from the clavicle to the caudal aspect of the right mandibular ramus. Blunt dissection through the subcutaneous layer was followed by lateral retraction of the sternomastoid, revealing the common carotid artery. The vagus nerve was dissected free from the common carotid artery. The common carotid was followed under the mandible to the bifurcations of the internal and external branches. A vascular clamp was placed on the external carotid branch to occlude it. Next, a 24G catheter was introduced into the common carotid artery. A controlled infusion (virus was diluted with sterile PBS to a final dose of 2E12 VGs) was performed over 10 min (200 μL/min). After the infusion, the vascular clamp was released and the catheter removed. Hemostasis was achieved with direct digital pressure. The skin incision was closed with continuous 4-0 Monocryl in the subcutis, and skin was apposed with continuous 4-0 intradermal Monocryl. Animals recovered on the operating room table until extubation; thereafter, they were returned to their home cage.

Neurological Rating Scale Assessment

Twenty-four NHP behaviors were rated cage-side in awake animals including horizontal and vertical ocular pursuit, treat retrieval with both forelimbs, ability to bear weight on both hindlimbs, posture, balance, startle response, as well as bradykinesia, dystonia, and chorea of each limb and trunk.[53] A score of 0 indicated a normal phenotype, whereas a score of 3 indicated severely abnormal phenotypic movements. All animals were evaluated using the rating scale prior to surgery to obtain baseline scores and once per week for the duration of the study by Dr. McBride, who was blind to the animals' treatment groups.

Necropsy and Tissue Collection

Mice

Mice were anesthetized with a solution of ketamine and xylazine (10 and 1 mg/mL, respectively) and perfused with 20 mL of a sterile 0.9% sodium chloride solution through the left ventricle of the heart. For VGC analyses (n = 3 per group), brains were extracted and sectioned coronally into 1-mm-thick slabs using a mouse brain matrix. Brain regions were carefully dissected from both hemispheres, and samples were immediately frozen in dry ice and stored at −80°C for further processing. Liver samples were also collected and immediately frozen in dry ice and stored at −80°C for further processing. For histology analyses (n = 5 per group), mice were perfused with 0.9% sterile saline followed by 4% paraformaldehyde (PFA) in 0.1 M phosphate buffer, and brains were post fixed overnight in 4% PFA. Following fixation in PFA, brains were transferred to a 30% sucrose solution for cryoprotection.

Rhesus Macaques

Animals were sedated with ketamine and then deeply anesthetized with sodium pentobarbital followed by exsanguination. Brain and spinal cord were perfused through the ascending carotid artery with 2 L of 0.9% saline. Brain was removed from the skull, placed into an ice-cold, steel brain matrix, and blocked into 4-mm-thick slabs in the coronal plane. Tissue punches used for VGC analyses (n = 2 monkeys per group) were obtained from cortical and subcortical regions from the left and right hemispheres and immediately frozen on dry ice. Cervical, thoracic, and lumbar spinal cord segments were carefully removed from the vertebral columns. Brain slabs and lumbar spinal cord were subsequently post fixed in 4% PFA for

48 h and cryoprotected in 30% sucrose for histological analyses (n = 2 monkeys per group). Peripheral tissues were collected and frozen immediately in liquid nitrogen.

IF and Histochemistry

Cryoprotected tissue was sectioned at 40 μm on a freezing microtome. Sections were incubated overnight at room temperature with an antibody against GFP (1:1,000; Invitrogen) and for 1 h with an Alexa Fluor 488-conjugated secondary antibody (1:500; Invitrogen) as previously described.[53] Double labeling for GFP and IBA-1, GFAP, Olig2, CD31, or NeuN was completed with antibodies against GFP (1:1,000; Aves), IBA-1 (1:500; Wako), GFAP (1:1,000; Dako), Olig2 (1:500 mouse study [Abcam]; 1:500 monkey study [Millipore]), CD31 (1:50; Abcam), and NeuN (1:500; Millipore) as previously described.[40] Alexa Fluor 488-conjugated secondary antibody was used to visualize GFP (1:500; Invitrogen), and Alexa Fluor 546-conjugated secondary antibody (1:500; Invitrogen) visualized the second antigen. Following immunostaining, all sections were counterstained with Hoechst 33342 (1:10,000; Invitrogen). Images for Figures 1 and 3 were taken on an Olympus BX51 microscope with an Olympus DP72 camera controlled by CellSens program. For whole-brain mouse images, four images were taken at ×4 magnification and montaged together. All ×4 mouse images taken with the Olympus microscope used the same laser setting and an exposure time of 139.4 ms. All ×20 mouse images used the same laser setting and an exposure time of 27.54 ms. For double-labeled fluorescence of both mouse and NHP tissues, a Leica SP5 confocal microscope was used, along with the corresponding LAS AF program. The gain and exposure parameters were optimized for each image. For Figure 4 and EGFP/Hoechst cell counting of NHP brain regions, images were captured on an Olympus VS120 Slide scanner using an Olympus BX61VS microscope with a ×20 objective and a Hamamatsu C13440 Monochrome camera. Fifteen z stacks throughout the tissue were captured using an exposure time of 14.82 ms for the blue channel (Hoechst) and 45 ms for the green channel (GFP). Following capture, the z stacks were processed using a maximum intensity Z-projection in the CellSens program. Peripheral tissues were fixed in 10% neutral-buffered formalin, embedded in paraffin, sectioned at 5 μm, and stained with H&E (Leica ST5010 Autostainer XL; Leica Biosystems).

VGC Analysis

Mouse and NHP samples were processed for total DNA, RNA, and protein using the All Prep Kit (QIAGEN). 100 ng of total DNA was analyzed by qPCR using primer/probe sets specific for both vector DNA and genomic DNA on a QuantStudio 12K Flex (Applied Biosystems). The copy numbers of both the vector and genomic DNA were quantified by comparing with a standard curve generated from known amounts of DNA amplicons. VGs per cell were calculated by dividing total VGs by diploid copies of the glucagon (mouse) or albumin (rhesus) gene. The following primer sets were used: CAG promoter: forward 5′-CCACGTTCTGCTTCACTCTC-3′, reverse 5′-CCATCGCTGCACAAAATAATTAAAA, probe 5′-CCCCTCC CACCCCCAATTTT-3′; mouse glucagon gene: forward 5′-GA GGACCCTGATGAGATGAATG-3′, reverse 5′-GGAGTCCAGGTA TTTGCTGTAG, probe 5′-CCACTCACAGGGCACATTCACCA G-3′; rhesus albumin gene: forward 5′-GTGGGCTGTAATCAT GGTCTAG, reverse 5′-CTGCCGGTTCTCTTTCATTG, probe: 5′-AT GTCCACACAAATCTCTCCCTGGC.

GFP$^+$ and Hoechst$^+$ Cell Counts

Z-projected images of GFP$^+$ and Hoechst$^+$ fluorescently labeled coronal brain sections containing the dorsolateral pre-motor cortex, orbitofrontal cortex, and putamen were counted using the Olympus cellSens program. For each brain region quantified, a 40 × 40 grid was placed on the outlined brain region at low magnification using cellSens software. One box per each of the 40 rows was used to manually quantify the number of GFP$^+$ cells and Hoechst$^+$ cells (high magnification). For each tissue section, an average of 5,000 Hoechst$^+$ cells were counted per brain region. In total, 2.5% of each image was counted. A random number generator was used to determine which box to count in each of the 40 rows. In cases where the box lay over a tissue punch (collected for VGC analysis), another square from the same row was chosen using a random number generator. Two tissue sections spaced 480 μm apart from each other, and matched between animals, were used for the quantification of each brain region from all animals. For analysis, a ratio of GFP$^+$ cells (AAV-PHP.B-transduced cells) to Hoechst$^+$ cells (total cells) for each section was averaged between the two sections counted.

Statistical Analyses

All statistical analyses were performed with Prism software by GraphPad. Mouse brain VGC data were analyzed by: (1) a two-way ANOVA with injection route and brain region as the independent variables, and VGC as the dependent variable for the injection route comparison; and (2) a two-way ANOVA with dose and brain region as the independent variables and VGC as the dependent variable for the dosing comparison. When significant overall effects were found, Tukey's multiple comparison post hoc analyses were performed. Mouse peripheral tissue data were analyzed by a one-way ANOVA with injection route as the independent variable and VGCs as the dependent variable. Upon significant overall ANOVA effects, Tukey's multiple comparisons tests were made. NHP brain, spinal cord, and peripheral tissue VGC data, as well as GFP$^+$/Hoechst$^+$ cell count data, were assessed via planned t tests comparing the two injection routes in each region. In all cases, a p value <0.05 was considered significant.

Image Preparation

All graphs were made in Prism by GraphPad, and images were prepared in Microsoft PowerPoint and Adobe Illustrator.

SUPPLEMENTAL INFORMATION

Supplemental Information can be found online at https://doi.org/10.1016/j.ymthe.2019.07.017.

AUTHOR CONTRIBUTIONS

Study Design: W.A.L., J.S.D., and J.L.M.; Surgical Delivery of AAVs: W.A.L., Y.W., D.B., B.D.D., J.S.D., and J.L.M.; Necropsy and Tissue Collection: W.A.L., Y.W., D.B., B.D.D., J.S.D., and J.L.M.; Histology

and Microscopy: W.A.L., S.S., Y.W., D.B., J.S.D., B.D.D., and J.L.M.; Molecular Analysis: J.S.D., W.A.L., and J.L.M.; Statistical Analysis: W.A.L., J.S.D., and J.L.M.; Figure Preparation: W.A.L., S.S., J.S.D., and J.L.M.; and Manuscript Preparation: W.A.L., J.S.D., and J.L.M.

CONFLICTS OF INTEREST

J.L.M. has previously been a paid consultant for Spark Therapeutics and is currently a paid consultant for Takeda Pharmaceutical Company. J.L.M. is also currently receiving financial compensation for consulting with investigators at Rush University Medical Center and The University at Albany-SUNY regarding an award funded via the Michael J. Fox Foundation for Parkinson's Research. All other authors declare no competing interests.

ACKNOWLEDGMENTS

We thank Drs. Ben Deverman and Viviana Gradinaru for their generous use of the pAAV.PHP.B-EGFP plasmids. We thank Christoph Kahl and Michelle Gomes in the OHSU MVSC Core for production of the recombinant AAV-PHP.B viral vectors. We thank the ONPRC Small Laboratory Animals Unit and the Division of Comparative Medicine for the outstanding care of our mice and rhesus macaques, with special thanks to Darla Jacobs, Lauren Drew Martin, and Theodore Hobbs. We thank the ONPRC Pathology Unit for their expertise and assistance with necropsy and pathology. Finally, we thank Dr. Alison Weiss for her thoughtful edits on this manuscript. This research was supported by NIH Award NS099136 (J.L.M.) and The Bev Hartig Huntington's Disease Foundation (J.L.M.). This work was also supported by the Integrated Pathology Core at the ONPRC, which is supported by NIH Core Grant P51OD011092 and NIH Instrumentation Grant 1S10OD025002-01.

REFERENCES

1. Hocquemiller, M., Giersch, L., Audrain, M., Parker, S., and Cartier, N. (2016). Adeno-Associated Virus-Based Gene Therapy for CNS Diseases. Hum. Gene Ther. *27*, 478–496.
2. Aschauer, D.F., Kreuz, S., and Rumpel, S. (2013). Analysis of transduction efficiency, tropism and axonal transport of AAV serotypes 1, 2, 5, 6, 8 and 9 in the mouse brain. PLoS ONE *8*, e76310.
3. Dodiya, H.B., Bjorklund, T., Stansell, J., 3rd, Mandel, R.J., Kirik, D., and Kordower, J.H. (2010). Differential transduction following basal ganglia administration of distinct pseudotyped AAV capsid serotypes in nonhuman primates. Mol. Ther. *18*, 579–587.
4. Castle, M.J., Turunen, H.T., Vandenberghe, L.H., and Wolfe, J.H. (2016). Controlling AAV Tropism in the Nervous System with Natural and Engineered Capsids. Methods Mol. Biol. *1382*, 133–149.
5. Burger, C., Gorbatyuk, O.S., Velardo, M.J., Peden, C.S., Williams, P., Zolotukhin, S., Reier, P.J., Mandel, R.J., and Muzyczka, N. (2004). Recombinant AAV viral vectors pseudotyped with viral capsids from serotypes 1, 2, and 5 display differential efficiency and cell tropism after delivery to different regions of the central nervous system. Mol. Ther. *10*, 302–317.
6. Mingozzi, F., and High, K.A. (2011). Therapeutic in vivo gene transfer for genetic disease using AAV: progress and challenges. Nat. Rev. Genet. *12*, 341–355.
7. McCarty, D.M., Young, S.M., Jr., and Samulski, R.J. (2004). Integration of adeno-associated virus (AAV) and recombinant AAV vectors. Annu. Rev. Genet. *38*, 819–845.
8. Gil-Farina, I., Fronza, R., Kaeppel, C., Lopez-Franco, E., Ferreira, V., D'Avola, D., Benito, A., Prieto, J., Petry, H., Gonzalez-Aseguinolaza, G., and Schmidt, M. (2016). Recombinant AAV Integration Is Not Associated With Hepatic Genotoxicity in Nonhuman Primates and Patients. Mol. Ther. *24*, 1100–1105.
9. Sehara, Y., Fujimoto, K.I., Ikeguchi, K., Katakai, Y., Ono, F., Takino, N., Ito, M., Ozawa, K., and Muramatsu, S.I. (2017). Persistent Expression of Dopamine-Synthesizing Enzymes 15 Years After Gene Transfer in a Primate Model of Parkinson's Disease. Hum. Gene Ther. Clin. Dev. *28*, 74–79.
10. Wright, J.F., Le, T., Prado, J., Bahr-Davidson, J., Smith, P.H., Zhen, Z., Sommer, J.M., Pierce, G.F., and Qu, G. (2005). Identification of factors that contribute to recombinant AAV2 particle aggregation and methods to prevent its occurrence during vector purification and formulation. Mol. Ther. *12*, 171–178.
11. Wright, J.F. (2008). Manufacturing and characterizing AAV-based vectors for use in clinical studies. Gene Ther. *15*, 840–848.
12. Robert, M.A., Chahal, P.S., Audy, A., Kamen, A., Gilbert, R., and Gaillet, B. (2017). Manufacturing of recombinant adeno-associated viruses using mammalian expression platforms. Biotechnol. J. *12*, e1600193.
13. Leone, P., Shera, D., McPhee, S.W., Francis, J.S., Kolodny, E.H., Bilaniuk, L.T., Wang, D.J., Assadi, M., Goldfarb, O., Goldman, H.W., et al. (2012). Long-term follow-up after gene therapy for canavan disease. Sci. Transl. Med. *4*, 165ra163.
14. Niethammer, M., Tang, C.C., LeWitt, P.A., Rezai, A.R., Leehey, M.A., Ojemann, S.G., Flaherty, A.W., Eskandar, E.N., Kostyk, S.K., Sarkar, A., et al. (2017). Long-term follow-up of a randomized AAV2-*GAD* gene therapy trial for Parkinson's disease. JCI Insight *2*, e90133.
15. LeWitt, P.A., Rezai, A.R., Leehey, M.A., Ojemann, S.G., Flaherty, A.W., Eskandar, E.N., Kostyk, S.K., Thomas, K., Sarkar, A., Siddiqui, M.S., et al. (2011). AAV2-GAD gene therapy for advanced Parkinson's disease: a double-blind, sham-surgery controlled, randomised trial. Lancet Neurol. *10*, 309–319.
16. Mittermeyer, G., Christine, C.W., Rosenbluth, K.H., Baker, S.L., Starr, P., Larson, P., Kaplan, P.L., Forsayeth, J., Aminoff, M.J., and Bankiewicz, K.S. (2012). Long-term evaluation of a phase 1 study of AADC gene therapy for Parkinson's disease. Hum. Gene Ther. *23*, 377–381.
17. Marks, W.J., Jr., Baumann, T.L., and Bartus, R.T. (2016). Long-Term Safety of Patients with Parkinson's Disease Receiving rAAV2-Neurturin (CERE-120) Gene Transfer. Hum. Gene Ther. *27*, 522–527.
18. Rafii, M.S., Baumann, T.L., Bakay, R.A., Ostrove, J.M., Siffert, J., Fleisher, A.S., Herzog, C.D., Barba, D., Pay, M., Salmon, D.P., et al. (2014). A phase1 study of stereotactic gene delivery of AAV2-NGF for Alzheimer's disease. Alzheimers Dement. *10*, 571–581.
19. Worgall, S., Sondhi, D., Hackett, N.R., Kosofsky, B., Kekatpure, M.V., Neyzi, N., Dyke, J.P., Ballon, D., Heier, L., Greenwald, B.M., et al. (2008). Treatment of late infantile neuronal ceroid lipofuscinosis by CNS administration of a serotype 2 adeno-associated virus expressing CLN2 cDNA. Hum. Gene Ther. *19*, 463–474.
20. Tardieu, M., Zérah, M., Gougeon, M.L., Ausseil, J., de Bournonville, S., Husson, B., Zafeiriou, D., Parenti, G., Bourget, P., Poirier, B., et al. (2017). Intracerebral gene therapy in children with mucopolysaccharidosis type IIIB syndrome: an uncontrolled phase 1/2 clinical trial. Lancet Neurol. *16*, 712–720.
21. Russell, S., Bennett, J., Wellman, J.A., Chung, D.C., Yu, Z.F., Tillman, A., Wittes, J., Pappas, J., Elci, O., McCague, S., et al. (2017). Efficacy and safety of voretigene neparvovec (AAV2-hRPE65v2) in patients with RPE65-mediated inherited retinal dystrophy: a randomised, controlled, open-label, phase 3 trial. Lancet *390*, 849–860.
22. Foust, K.D., Nurre, E., Montgomery, C.L., Hernandez, A., Chan, C.M., and Kaspar, B.K. (2009). Intravascular AAV9 preferentially targets neonatal neurons and adult astrocytes. Nat. Biotechnol. *27*, 59–65.
23. Walia, J.S., Altaleb, N., Bello, A., Kruck, C., LaFave, M.C., Varshney, G.K., Burgess, S.M., Chowdhury, B., Hurlbut, D., Hemming, R., et al. (2015). Long-term correction of Sandhoff disease following intravenous delivery of rAAV9 to mouse neonates. Mol. Ther. *23*, 414–422.
24. Fu, H., Dirosario, J., Killedar, S., Zaraspe, K., and McCarty, D.M. (2011). Correction of neurological disease of mucopolysaccharidosis IIIB in adult mice by rAAV9 trans-blood-brain barrier gene delivery. Mol. Ther. *19*, 1025–1033.
25. Bosch, M.E., Aldrich, A., Fallet, R., Odvody, J., Burkovetskaya, M., Schuberth, K., Fitzgerald, J.A., Foust, K.D., and Kielian, T. (2016). Self-Complementary AAV9 Gene Delivery Partially Corrects Pathology Associated with Juvenile Neuronal Ceroid Lipofuscinosis (CLN3). J. Neurosci. *36*, 9669–9682.

26. Haurigot, V., Marcó, S., Ribera, A., Garcia, M., Ruzo, A., Villacampa, P., Ayuso, E., Añor, S., Andaluz, A., Pineda, M., et al. (2013). Whole body correction of mucopolysaccharidosis IIIA by intracerebrospinal fluid gene therapy. J. Clin. Invest. *123*, 3254–3271.

27. Hughes, M.P., Smith, D.A., Morris, L., Fletcher, C., Colaco, A., Huebecker, M., Tordo, J., Palomar, N., Massaro, G., Henckaerts, E., et al. (2018). AAV9 intracerebroventricular gene therapy improves lifespan, locomotor function and pathology in a mouse model of Niemann-Pick type C1 disease. Hum. Mol. Genet. *27*, 3079–3098.

28. Laoharawee, K., Podetz-Pedersen, K.M., Nguyen, T.T., Evenstar, L.B., Kitto, K.F., Nan, Z., Fairbanks, C.A., Low, W.C., Kozarsky, K.F., and McIvor, R.S. (2017). Prevention of Neurocognitive Deficiency in Mucopolysaccharidosis Type II Mice by Central Nervous System-Directed, AAV9-Mediated Iduronate Sulfatase Gene Transfer. Hum. Gene Ther. *28*, 626–638.

29. Mitchell, N.L., Russell, K.N., Wellby, M.P., Wicky, H.E., Schoderboeck, L., Barrell, G.K., Melzer, T.R., Gray, S.J., Hughes, S.M., and Palmer, D.N. (2018). Longitudinal In Vivo Monitoring of the CNS Demonstrates the Efficacy of Gene Therapy in a Sheep Model of CLN5 Batten Disease. Mol. Ther. *26*, 2366–2378.

30. Gadalla, K.K., Bailey, M.E., Spike, R.C., Ross, P.D., Woodard, K.T., Kalburgi, S.N., Bachaboina, L., Deng, J.V., West, A.E., Samulski, R.J., et al. (2013). Improved survival and reduced phenotypic severity following AAV9/MECP2 gene transfer to neonatal and juvenile male Mecp2 knockout mice. Mol. Ther. *21*, 18–30.

31. Garg, S.K., Lioy, D.T., Cheval, H., McGann, J.C., Bissonnette, J.M., Murtha, M.J., Foust, K.D., Kaspar, B.K., Bird, A., and Mandel, G. (2013). Systemic delivery of MeCP2 rescues behavioral and cellular deficits in female mouse models of Rett syndrome. J. Neurosci. *33*, 13612–13620.

32. Benkhelifa-Ziyyat, S., Besse, A., Roda, M., Duque, S., Astord, S., Carcenac, R., Marais, T., and Barkats, M. (2013). Intramuscular scAAV9-SMN injection mediates widespread gene delivery to the spinal cord and decreases disease severity in SMA mice. Mol. Ther. *21*, 282–290.

33. Shababi, M., Feng, Z., Villalon, E., Sibigtroth, C.M., Osman, E.Y., Miller, M.R., Williams-Simon, P.A., Lombardi, A., Sass, T.H., Atkinson, A.K., et al. (2016). Rescue of a Mouse Model of Spinal Muscular Atrophy With Respiratory Distress Type 1 by AAV9-IGHMBP2 Is Dose Dependent. Mol. Ther. *24*, 855–866.

34. Shababi, M., Villalón, E., Kaifer, K.A., DeMarco, V., and Lorson, C.L. (2018). A Direct Comparison of IV and ICV Delivery Methods for Gene Replacement Therapy in a Mouse Model of SMARD1. Mol. Ther. Methods Clin. Dev. *10*, 348–360.

35. Meyer, K., Ferraiuolo, L., Schmelzer, L., Braun, L., McGovern, V., Likhite, S., Michels, O., Govoni, A., Fitzgerald, J., Morales, P., et al. (2015). Improving single injection CSF delivery of AAV9-mediated gene therapy for SMA: a dose-response study in mice and nonhuman primates. Mol. Ther. *23*, 477–487.

36. Stoica, L., Todeasa, S.H., Cabrera, G.T., Salameh, J.S., ElMallah, M.K., Mueller, C., Brown, R.H., Jr., and Sena-Esteves, M. (2016). Adeno-associated virus-delivered artificial microRNA extends survival and delays paralysis in an amyotrophic lateral sclerosis mouse model. Ann. Neurol. *79*, 687–700.

37. Foust, K.D., Salazar, D.L., Likhite, S., Ferraiuolo, L., Ditsworth, D., Ilieva, H., Meyer, K., Schmelzer, L., Braun, L., Cleveland, D.W., and Kaspar, B.K. (2013). Therapeutic AAV9-mediated suppression of mutant SOD1 slows disease progression and extends survival in models of inherited ALS. Mol. Ther. *21*, 2148–2159.

38. Yamashita, T., Chai, H.L., Teramoto, S., Tsuji, S., Shimazaki, K., Muramatsu, S., and Kwak, S. (2013). Rescue of amyotrophic lateral sclerosis phenotype in a mouse model by intravenous AAV9-ADAR2 delivery to motor neurons. EMBO Mol. Med. *5*, 1710–1719.

39. He, Y., Pan, S., Xu, M., He, R., Huang, W., Song, P., Huang, J., Zhang, H.T., and Hu, Y. (2017). Adeno-associated virus 9-mediated Cdk5 inhibitory peptide reverses pathologic changes and behavioral deficits in the Alzheimer's disease mouse model. FASEB J. *31*, 3383–3392.

40. Dufour, B.D., Smith, C.A., Clark, R.L., Walker, T.R., and McBride, J.L. (2014). Intrajugular vein delivery of AAV9-RNAi prevents neuropathological changes and weight loss in Huntington's disease mice. Mol. Ther. *22*, 797–810.

41. Deverman, B.E., Pravdo, P.L., Simpson, B.P., Kumar, S.R., Chan, K.Y., Banerjee, A., Wu, W.L., Yang, B., Huber, N., Pasca, S.P., and Gradinaru, V. (2016). Cre-dependent selection yields AAV variants for widespread gene transfer to the adult brain. Nat. Biotechnol. *34*, 204–209.

42. Guillaume, D.J., Doolittle, N.D., Gahramanov, S., Hedrick, N.A., Delashaw, J.B., and Neuwelt, E.A. (2010). Intra-arterial chemotherapy with osmotic blood-brain barrier disruption for aggressive oligodendroglial tumors: results of a phase I study. Neurosurgery *66*, 48–58, discussion 58.

43. Jahnke, K., Kraemer, D.F., Knight, K.R., Fortin, D., Bell, S., Doolittle, N.D., Muldoon, L.L., and Neuwelt, E.A. (2008). Intraarterial chemotherapy and osmotic blood-brain barrier disruption for patients with embryonal and germ cell tumors of the central nervous system. Cancer *112*, 581–588.

44. Ahn, S.J., Kim, H.C., Chung, J.W., An, S.B., Yin, Y.H., Jae, H.J., and Park, J.H. (2012). Ultrasound and fluoroscopy-guided placement of central venous ports via internal jugular vein: retrospective analysis of 1254 port implantations at a single center. Korean J. Radiol. *13*, 314–323.

45. Federici, T., Taub, J.S., Baum, G.R., Gray, S.J., Grieger, J.C., Matthews, K.A., Handy, C.R., Passini, M.A., Samulski, R.J., and Boulis, N.M. (2012). Robust spinal motor neuron transduction following intrathecal delivery of AAV9 in pigs. Gene Ther. *19*, 852–859.

46. Hirai, T., Enomoto, M., Machida, A., Yamamoto, M., Kuwahara, H., Tajiri, M., Hirai, Y., Sotome, S., Mizusawa, H., Shinomiya, K., et al. (2012). Intrathecal shRNA-AAV9 inhibits target protein expression in the spinal cord and dorsal root ganglia of adult mice. Hum. Gene Ther. Methods *23*, 119–127.

47. Passini, M.A., Bu, J., Richards, A.M., Treleaven, C.M., Sullivan, J.A., O'Riordan, C.R., Scaria, A., Kells, A.P., Samaranch, L., San Sebastian, W., et al. (2014). Translational fidelity of intrathecal delivery of self-complementary AAV9-survival motor neuron 1 for spinal muscular atrophy. Hum. Gene Ther. *25*, 619–630.

48. Sinnett, S.E., Hector, R.D., Gadalla, K.K.E., Heindel, C., Chen, D., Zaric, V., Bailey, M.E.S., Cobb, S.R., and Gray, S.J. (2017). Improved *MECP2* Gene Therapy Extends the Survival of MeCP2-Null Mice without Apparent Toxicity after Intracisternal Delivery. Mol. Ther. Methods Clin. Dev. *5*, 106–115.

49. Castle, M.J., Cheng, Y., Asokan, A., and Tuszynski, M.H. (2018). Physical positioning markedly enhances brain transduction after intrathecal AAV9 infusion. Sci. Adv *4*, eaau9859.

50. Hordeaux, J., Hinderer, C., Goode, T., Buza, E.L., Bell, P., Calcedo, R., Richman, L.K., and Wilson, J.M. (2018). Toxicology Study of Intra-Cisterna Magna Adeno-Associated Virus 9 Expressing Iduronate-2-Sulfatase in Rhesus Macaques. Mol. Ther. Methods Clin. Dev. *10*, 68–78.

51. Hordeaux, J., Hinderer, C., Goode, T., Katz, N., Buza, E.L., Bell, P., Calcedo, R., Richman, L.K., and Wilson, J.M. (2018). Toxicology Study of Intra-Cisterna Magna Adeno-Associated Virus 9 Expressing Human Alpha-L-Iduronidase in Rhesus Macaques. Mol. Ther. Methods Clin. Dev. *10*, 79–88.

52. Marshall, M.S., Issa, Y., Jakubauskas, B., Stoskute, M., Elackattu, V., Marshall, J.N., Bogue, W., Nguyen, D., Hauck, Z., Rue, E., et al. (2018). Long-Term Improvement of Neurological Signs and Metabolic Dysfunction in a Mouse Model of Krabbe's Disease after Global Gene Therapy. Mol. Ther. *26*, 874–889.

53. McBride, J.L., Pitzer, M.R., Boudreau, R.L., Dufour, B., Hobbs, T., Ojeda, S.R., and Davidson, B.L. (2011). Preclinical safety of RNAi-mediated HTT suppression in the rhesus macaque as a potential therapy for Huntington's disease. Mol. Ther. *19*, 2152–2162.

54. Okuyama, S., Okuyama, J., Okuyama, J., Tamatsu, Y., Shimada, K., Hoshi, H., and Iwai, J. (2004). The arterial circle of Willis of the mouse helps to decipher secrets of cerebral vascular accidents in the human. Med. Hypotheses *63*, 997–1009.

55. Liu, R., Martuza, R.L., and Rabkin, S.D. (2005). Intracarotid delivery of oncolytic HSV vector G47Delta to metastatic breast cancer in the brain. Gene Ther. *12*, 647–654.

56. Zincarelli, C., Soltys, S., Rengo, G., and Rabinowitz, J.E. (2008). Analysis of AAV serotypes 1-9 mediated gene expression and tropism in mice after systemic injection. Mol. Ther. *16*, 1073–1080.

57. Kotchey, N.M., Adachi, K., Zahid, M., Inagaki, K., Charan, R., Parker, R.S., and Nakai, H. (2011). A potential role of distinctively delayed blood clearance of recombinant adeno-associated virus serotype 9 in robust cardiac transduction. Mol. Ther. *19*, 1079–1089.

58. Shen, S., Bryant, K.D., Sun, J., Brown, S.M., Troupes, A., Pulicherla, N., and Asokan, A. (2012). Glycan binding avidity determines the systemic fate of adeno-associated virus type 9. J. Virol. *86*, 10408–10417.

59. Morabito, G., Giannelli, S.G., Ordazzo, G., Bido, S., Castoldi, V., Indrigo, M., Cabassi, T., Cattaneo, S., Luoni, M., Cancellieri, C., et al. (2017). AAV-PHP.B-Mediated

Global-Scale Expression in the Mouse Nervous System Enables GBA1 Gene Therapy for Wide Protection from Synucleinopathy. Mol. Ther. *25*, 2727–2742.

60. Colella, P., Ronzitti, G., and Mingozzi, F. (2017). Emerging Issues in AAV-Mediated *In Vivo* Gene Therapy. Mol. Ther. Methods Clin. Dev. *8*, 87–104.
61. Hinderer, C., Katz, N., Buza, E.L., Dyer, C., Goode, T., Bell, P., Richman, L.K., and Wilson, J.M. (2018). Severe Toxicity in Nonhuman Primates and Piglets Following High-Dose Intravenous Administration of an Adeno-Associated Virus Vector Expressing Human SMN. Hum. Gene Ther. *29*, 285–298.
62. Gruntman, A.M., Su, L., and Flotte, T.R. (2017). Retro-Orbital Venous Sinus Delivery of rAAV9 Mediates High-Level Transduction of Brain and Retina Compared with Temporal Vein Delivery in Neonatal Mouse Pups. Hum. Gene Ther. *28*, 228–230.
63. Hinderer, C., Bell, P., Vite, C.H., Louboutin, J.P., Grant, R., Bote, E., Yu, H., Pukenas, B., Hurst, R., and Wilson, J.M. (2014). Widespread gene transfer in the central nervous system of cynomolgus macaques following delivery of AAV9 into the cisterna magna. Mol. Ther. Methods Clin. Dev. *1*, 14051.
64. Samaranch, L., Salegio, E.A., San Sebastian, W., Kells, A.P., Bringas, J.R., Forsayeth, J., and Bankiewicz, K.S. (2013). Strong cortical and spinal cord transduction after AAV7 and AAV9 delivery into the cerebrospinal fluid of nonhuman primates. Hum. Gene Ther. *24*, 526–532.
65. Gray, S.J., Nagabhushan Kalburgi, S., McCown, T.J., and Jude Samulski, R. (2013). Global CNS gene delivery and evasion of anti-AAV-neutralizing antibodies by intrathecal AAV administration in non-human primates. Gene Ther. *20*, 450–459.
66. Gray, S.J., Matagne, V., Bachaboina, L., Yadav, S., Ojeda, S.R., and Samulski, R.J. (2011). Preclinical differences of intravascular AAV9 delivery to neurons and glia: a comparative study of adult mice and nonhuman primates. Mol. Ther. *19*, 1058–1069.
67. Bevan, A.K., Duque, S., Foust, K.D., Morales, P.R., Braun, L., Schmelzer, L., Chan, C.M., McCrate, M., Chicoine, L.G., Coley, B.D., et al. (2011). Systemic gene delivery in large species for targeting spinal cord, brain, and peripheral tissues for pediatric disorders. Mol. Ther. *19*, 1971–1980.
68. Samaranch, L., Salegio, E.A., San Sebastian, W., Kells, A.P., Foust, K.D., Bringas, J.R., Lamarre, C., Forsayeth, J., Kaspar, B.K., and Bankiewicz, K.S. (2012). Adeno-associated virus serotype 9 transduction in the central nervous system of nonhuman primates. Hum. Gene Ther. *23*, 382–389.
69. Matsuzaki, Y., Konno, A., Mochizuki, R., Shinohara, Y., Nitta, K., Okada, Y., and Hirai, H. (2018). Intravenous administration of the adeno-associated virus-PHP.B capsid fails to upregulate transduction efficiency in the marmoset brain. Neurosci. Lett. *665*, 182–188.
70. Hordeaux, J., Wang, Q., Katz, N., Buza, E.L., Bell, P., and Wilson, J.M. (2018). The Neurotropic Properties of AAV-PHP.B Are Limited to C57BL/6J Mice. Mol. Ther. *26*, 664–668.
71. Hordeaux, J., Yuan, Y., Clark, P.M., Wang, Q., Martino, R.A., Sims, J.J., Bell, P., Raymond, A., Stanford, W.L., and Wilson, J.M. (2019). The GPI-Linked Protein LY6A Drives AAV-PHP.B Transport across the Blood-Brain Barrier. Mol. Ther. *27*, 912–921.
72. Loughner, C.L., Bruford, E.A., McAndrews, M.S., Delp, E.E., Swamynathan, S., and Swamynathan, S.K. (2016). Organization, evolution and functions of the human and mouse Ly6/uPAR family genes. Hum. Genomics *10*, 10.
73. Shen, S., Bryant, K.D., Brown, S.M., Randell, S.H., and Asokan, A. (2011). Terminal N-linked galactose is the primary receptor for adeno-associated virus 9. J. Biol. Chem. *286*, 13532–13540.
74. Pillay, S., Meyer, N.L., Puschnik, A.S., Davulcu, O., Diep, J., Ishikawa, Y., Jae, L.T., Wosen, J.E., Nagamine, C.M., Chapman, M.S., and Carette, J.E. (2016). An essential receptor for adeno-associated virus infection. Nature *530*, 108–112.
75. McCarty, D.M. (2008). Self-complementary AAV vectors; advances and applications. Mol. Ther. *16*, 1648–1656.
76. Tervo, D.G., Hwang, B.Y., Viswanathan, S., Gaj, T., Lavzin, M., Ritola, K.D., Lindo, S., Michael, S., Kuleshova, E., Ojala, D., et al. (2016). A Designer AAV Variant Permits Efficient Retrograde Access to Projection Neurons. Neuron *92*, 372–382.
77. Naidoo, J., Stanek, L.M., Ohno, K., Trewman, S., Samaranch, L., Hadaczek, P., O'Riordan, C., Sullivan, J., San Sebastian, W., Bringas, J.R., et al. (2018). Extensive Transduction and Enhanced Spread of a Modified AAV2 Capsid in the Non-human Primate CNS. Mol. Ther. *26*, 2418–2430.